Impact of Predictor Variables on Estimates of Global Sea-Air CO_2 Fluxes Using an Extra Trees Machine Learning Approach

Rik Wanninkhof[1], Joaquin Triñanes[1,2,3], Denis Pierrot[1], David R. Munro[4,5], Colm Sweeney[4], and Amanda R. Fay[6]

[1]Atlantic Oceanographic and Meteorological Laboratory, National Oceanic and Atmospheric Administration, 4301 Rickenbacker Causeway, Miami, FL, USA.

[2]Cooperative Institute for Marine and Atmospheric Studies, Rosenstiel School of Marine, Atmospheric and Earth Science, University of Miami, 4600 Rickenbacker Causeway, Miami, FL, USA.

[3]Dept. of Electronics and Computer Science, Universidade de Santiago de Compostela, Santiago, Spain

[4]Global Monitoring Laboratory, National Oceanic and Atmospheric Administration, Boulder, CO, USA

[5]Cooperative Institute for Research in Environmental Sciences (CIRES), University of Colorado, Boulder, CO, USA

[6]Columbia University and Lamont Doherty Earth Observatory, Palisades NY, USA

Corresponding author: Rik Wanninkhof (rik.wanninkhof@noaa.gov)

†ORCID: 0000-0003-1973-3514.

Key Points:

- An Extra Trees machine learning approach, AOML_ET is described used to determine global sea-air CO_2 fluxes.
- Global sea-air CO_2 fluxes from 1998-2020 are -1.7 Pg C yr^{-1} with a trend of 0.9 Pg C $decade^{-1}$.
- Comparison with other approaches and using different predictor variables show good agreement in global fluxes but with large regional differences.

Abstract

Monthly global sea-air CO_2 flux estimates from 1998-2020 are produced by extrapolation of surface water fugacity of CO_2 (fCO_{2w}) observations using an Extra-trees (ET) machine learning technique. This new product (AOML_ET) is one of the eleven observation-based submissions to the second REgional Carbon Cycle Assessment and Processes (RECCAP2) effort. The target variable fCO_{2w} is derived using the predictor variables including date, location, sea surface temperature, mixed layer depth, and chlorophyll-a. A monthly resolved sea-air CO_2 flux product on a 1˚ by 1˚ grid is created from this fCO_{2w} product using a bulk flux formulation. Average global sea-air CO_2 fluxes from 1998-2020 are -1.7 Pg C yr^{-1} with a trend of 0.9 Pg C $decade^{-1}$. The sensitivity to omitting mixed layer depth or chlorophyll-a as predictors is small but changing the target variable from fCO_{2w} to air-water fCO_2 difference has a large effect, yielding an average flux of -3.6 Pg C yr^{-1} and a trend of 0.5 Pg C $decade^{-1}$. Substituting a spatially resolved marine air CO_2 mole fraction product for the commonly used zonally invariant marine boundary layer CO_2 product yield greater influx and less outgassing in the Eastern coastal regions of North America and Northern Asia but with no effect on the global fluxes. A comparison of AOML_ET for 2010 with an updated climatology following the methods of Takahashi et al. (2009), that extrapolates the surface CO_2 values without predictors, shows overall agreement in global patterns and magnitude.

Plain Language Summary

Surface water measurements of carbon dioxide (CO_2) are used to determine the global sea-air flux of CO_2 across the interface for the time period from 1998-2020. The global flux direction is into the ocean driven by atmospheric CO_2 increases caused by burning of fossil fuels and other anthropogenic activities which affects the balance of the sea-air CO_2 gradient. While an increasing number of surface ocean CO_2 observations are available, the data still requires significant extrapolation/gap filling to characterize the entire global surface ocean on a monthly basis. Here we describe a machine leaning (ML) approach to create a monthly resolved surface water CO_2 and flux product on a 1-degree grid using an extreme randomized trees or Extra Trees approach, referred to as AOML_ET. AOML_ET is one of eleven observation-based submissions to the second REgional Carbon Cycle Assessment and Processes (RECCAP2) effort. The global scale results are compared to other available products and the sensitivity to different predictor and target variables is described. Overall, there is strong agreement between approaches and sensitivity to omitting certain target variables is small suggesting that on global scales the approach is robust.

1 Introduction

Sea-air CO_2 fluxes are the main conduit for transfer and subsequent storage of anthropogenic CO_2 in the ocean. The resulting increases in surface water CO_2 are the cause of surface ocean acidification (Doney et al., 2020; Lida et al. 2021). Quantifying the fluxes is critical for the global stocktake which reviews progress towards the Paris Agreement goals every five years (Magnan et al., 2016), and to assess if the oceanic sink is changing on annual timescales, particularly in light of the societal goal of reaching “net zero” by 2050 (IPCC, 2018).

Most regional and global sea-air CO_2 flux estimates on seasonal to annual scales rely on using the bulk flux formulation where the flux density is the product of the gas transfer velocity, CO_2 solubility, and the fugacity difference of CO_2, or ΔfCO_2 between water (fCO_{2w}) and air (fCO_{2a})

(Eqn. 1). Here we use fCO_2 which accounts for the non-ideality of CO_2 gas rather than partial pressure of CO_2 (pCO_2), except in the discussion of the updated Takahashi climatology. Numerically fCO_2 =0.997 pCO_2 at 25 ˚C and the air-water fCO_2 difference, ΔfCO_2 is essentially the same as ΔpCO_2, such that the results expressed in terms of ΔpCO_2 can be directly compared. The gas transfer velocity is commonly parameterized as a quadratic dependence with wind speed (Wanninkhof, 2014). Surface water fCO_2 values are obtained using automated instrumentation on a variety of ships and other platforms, such as moorings and autonomous surface vehicles. The data are quality controlled and collated into communal data holdings, notably the Surface Ocean CO_2 Atlas, SOCAT (Bakker et al., 2016) that is updated annually with an increase of over 1 million unique datapoints for each iteration (https://www.socat.info/wp-content/uploads/2022/06/2022_Poster_SOCATv2022_release.pdf). The fCO_{2w} data are binned, gridded and interpolated/mapped to provide the foundation for global sea-air CO_2 flux fields, often referred to as CO_2 flux maps. The interpolation in space and time is critical to obtain uniform full coverage over the global ocean.

The initial interpolations of surface water pCO_2 data to estimate global sea-air CO_2 fluxes were performed by Taro Takahashi and colleagues who determined global monthly pCO_2 maps and a sea-air CO_2 flux climatology (Takahashi et al., 1997; 2009). The climatologies used much of the available pCO_2 data at the time normalized to a particular year and presented per month on a 4˚ by 5˚ grid. The empty cells were filled through interpolation to its neighbors aided by a modelled surface ocean advection scheme (Bryan & Lewis, 1979). Here we present the Takahashi climatology as submitted to RECCAP2 that is centered on reference year 2010, henceforth referred to as Tak-2010. This climatology was recently updated by Fay et al. (2023, submitted) using the same scheme and assumptions but with a larger dataset, the SOCATv2022 data product. The climatology using a greater dataset and different approach for accounting for fCO_{2w} increase through time by Fay et al. (2023) shows the same monthly spatial patterns and a global flux of -1.79 ± 0.6 Pg C in close agreement with Tak-2010 results presented here of -1.86 ± 0.52 Pg C. The Tak-2010 climatology, that is part of the RECCAP2 observation-based data holdings, is chosen as a comparison in this study as it differs from other interpolation schemes in that the pCO_2 data is interpolated/mapped without use of predictor variables. This is in contrast to the various machine learning (ML) and linear regression approaches that rely heavily on the predictor variables (Rödenbeck et al., 2015).

Much of the efforts in creating global sea-air CO_2 flux estimates have focused on approaches to map fCO_{2w} and subsequent comparisons and syntheses of the methods (Telszewski et al., 2009; Landschützer et al., 2013; Zeng et al., 2014; Gregor et al., 2019; Stamell et al., 2020; Fay et al., 2021). Significant improvement in these observation-based approaches have been made in the last decade (Rödenbeck et al., 2015) notably through use of ML approaches for interpolation/mapping of fCO_{2w} along with an increase in available surface water measurements. The products are commonly presented per month at 1˚ by 1˚ spatial resolution. These scales are on the order of the autocorrelation scales of fCO_{2w} (Li et al., 2005). The RECCAP2 analyses include the output of eleven of such approaches with consistent protocols for nomenclature and analysis. The recommended time range for the RECCAP2 surface water analysis spans years from 1985-2018. The product described here covers the time period from October 1997 through December 2020. The later start date is chosen because both the sparsity of fCO_{2w} data, and the

inconsistent quality and coverage of predictor variables until the late 90s, most notably remotely sensed chlorophyll estimates which became available from a common source at the end of 1997.

The extremely randomized trees or Extra Trees method (ET) used here (AOML_ET) is one of several ML and regression approaches that use the same community assembled SOCAT database. The SOCATv2020 product includes over 33 million unique fCO_{2w} observations collected from 1957 through 2021(www.socat.info). However, for this analysis the gridded SOCAT data product is used which consists of data collated into monthly 1˚ by 1˚ cells, reducing the total to approximately 309 thousand data points. The eleven observation-based approaches included in RECCAP2 regress the fCO_{2w} from predictor variables, or use the predictor variables in the training step of a ML technique. Interpolation is required due to sparse coverage of the gridded SOCAT data product which has significant temporal and spatial gaps at the 1˚ by 1˚ monthly resolution, particularly in the remote sections of the oceans and in winter seasons in the mid- and high latitude oceans. Indeed, only about 2 % of the monthly 1˚ by 1˚ cells have fCO_{2w} observations (Stamell et al., 2020). Predictor variables vary amongst approaches but surface fCO_{2w} values have been seen to closely correlate with sea surface temperature (SST) and mixed layer depth (MLD). Sea surface salinity (SSS) and Chlorophyll-a (Chl-a) are often used as well. These variables are known to directly influence fCO_{2w} through biogeochemical and physical interactions that control fCO_{2w}. Location (latitude, longitude) and time (yearday) are included in the AOML_ET method to facilitate depiction of regional differences and trends. Atmospheric mixing ratio of CO_2 (XCO_{2a}) has been used by other ML approaches as a time dependent variable (e.g. Landschützer et al., 2016). Clustering or bagging approaches and delineation of regions in specific biogeographical provinces or biomes (e.g. Fay & McKinley, 2014) have aided the training and mapping in some ML and regression approaches but are not used in AOML_ET.

Different ML methods and other mapping products have been compared notably under the aegis of the Surface Ocean CO_2 Mapping intercomparisons (SOCOM) effort (Rödenbeck et al., 2015) and used in several assessments, including the global ocean carbon RECCAP2 effort (DeVries et al., 2023). Detailed regional and global comparisons of different mapping products and ensemble approaches have been undertaken (e.g. Fay et al., 2021; Gregor et al., 2019; Rödenbeck et al., 2022; Chau et al., 2022). The analysis by Gregor et al. (2019) includes several different ML approaches and suggests that overall skill of the methods at the global scale is similar and that the skill for any given approach is mainly limited by fCO_{2w} data availability in undersampled regions and seasons. Gregor et al. (2019) also show broad similarity in magnitude and interannual variability of fCO_{2w} for the various ML approaches. In particular, the Northern Hemisphere oceans show agreement between methods while areas with fewer fCO_{2w} observations such as the mid- and high-latitude Southern Hemisphere oceans, and regions with large interannual variability such as the Equatorial Pacific show greater differences between approaches. Inconsistencies in modeled surface areas, wind speed products and the method of calculation of fluxes contribute to differences. To account for these differences area normalization and ensembles (or multi-product averages) are increasingly common in intercomparison studies and improve consistency (Fay et al., 2021; Roobaert et al., 2018). A summary of the annual global sea-air CO_2 fluxes for different ML approaches used in the Global Carbon Budget (Friedlingstein et al., 2022) is provided in Figure 1 that show correspondence over time between the observation-based methods at the global scale.

To date comparisons have often focused on the differences in the mapped fCO_{2w} fields for the different ML approaches, and the sea-air CO_2 fluxes derived from these fields using standard indicators such as root mean square error (RMSE), bias, and the ability of the methods to reproduce seasonal and interannual variability and trends at global and basin scales (Rödenbeck et al., 2015; Gregor et al., 2019). Differences in flux products from other parameters used in the bulk flux equation such as the gas transfer parameterization, as well as the sensitivity to different predictor variables have been explored to lesser extent. The ET approach used here is computationally efficient so that it lends itself to exploration of the impact of different variables. Potential drawbacks of the ET method include that it can be more prone to bias in data sparse regions compared to other ML methods. More specifically, with the ET approach observations in regions with few data are viewed as outliers such that adjacent data further removed in time and space receive greater weight (Gregor et al., 2019). It also shows a greater sensitivity to overfitting than other commonly used ML approaches (Stamell et al., 2020; Gregor et al., 2019).

The paper is structured as follows: in the methods section we lay out the approach to determine the sea-air CO_2 flux using the bulk flux formulation. The mapping of monthly fCO_{2w} fields is described using the analysis called AOML_EXTRAT_1998-2020, or AOML_ET for short. This serves in part as documentation for the product submitted to RECCAP2. Of note is that the AOML_ET RECCAP2 submission covers the time period 1998-2018 and this analysis is extended by two years using the same procedures but with an updated SOCAT gridded dataset (SOCATv2021). Different adaptions and predictor /target variables are described. The discussion focusses on the seasonal and regional patterns observed in the AOML_ET product using an analyses spanning a 22-year time series. A comparison with an updated climatology based on the methods of Takahashi et al. (2009), Tak-2010, that was also submitted to RECCAP2 (DeVries et al., 2023) is included. This climatological product is centered on 2010 and uses SOCAT data from 1985-2018. The sensitivity of predictors to develop the fCO_{2w} fields in AOML_ET approach is discussed. Two different estimates of the mole fraction of CO_2 in air (XCO_{2a}) are applied to determine the sensitivity of sea-air CO_2 fluxes to XCO_{2a}. The zonal-mean MBL reference surface (MBL-RS) (Dlugokencky et al., 2021) that is used in many previous global CO_2 flux estimates, including RECCAP2, is compared with the XCO_{2a} derived from an atmospheric CO_2 model, Carbon Tracker (Jacobson et al., 2020). The impact of two different gas transfer-wind speed formulations is provided to illustrate the impact of the kinetic forcing of fluxes which are not always considered when comparing the agreements of different sea-air CO_2 flux products. Some large scale diagnostics for sea-air fugacity difference and fluxes are also presented. Fluxes presented are net CO_2 fluxes.

2 Methodology

2.1 Determination of fluxes

The fCO_{2w} measurements are the foundation for determining the sea-air CO_2 fluxes but flux estimates require other inputs such as the rate of CO_2 transfer across the sea-air interface and CO_2 air concentrations as well. The sea-air CO_2 fluxes on regional to global scales are determined using a bulk flux formulation where the flux density (F_{sa}) is defined as the product of a thermodynamic term, the gradient across the interface (ΔfCO_2), and a kinetic term, the gas transfer velocity (k). The interpolation and gap filling methods focus on creating fCO_{2w} fields,

and use canonical estimates for fCO_{2a} and gas transfer parameterizations. The following expression for the bulk flux equation is applicable:

$$F_{sa} = \overline{k\, K_0\, (fCO_{2w} - fCO_{2a})} = \overline{k\, K_0\, \Delta fCO_2} \quad (1)$$

where K_0 is the solubility of CO_2 in seawater. The ΔfCO_2 is the difference between the fugacity that would be in equilibrium with water at 1 to 6 m below the interface, fCO_{2w} and air, fCO_{2a}. The fCO_{2a} is derived from a latitudinal averaged time series of mole fraction XCO_{2a} of the marine boundary layer, MBL-RS (Dlugokencky et al., 2021). The overbar depicts the integrated quantity.

When calculating flux densities, the monthly ΔfCO_2 fields at 1˚ by 1˚ grid are multiplied by the product of gas transfer velocity and solubility, thereby changing Eqn. (1) to:

$$F_{sa} = \overline{k\, K_0}\; \overline{\Delta fCO_2} \quad (2)$$

The Taylor expansion from the average of the product to averages of the individual terms has cross-correlation terms of k' and ΔfCO_2' but they are not included as they have a small influence on the overall results for determination of monthly global fluxes on scales of 1˚ (Wanninkhof et al., 2011).

The k is commonly parameterized as the square of wind speed (Wanninkhof et al., 2009):

$$k = 0.251 \langle u^2 \rangle (Sc/660)^{-1/2} \quad \text{or } k_{660} = 0.251 \langle u^2 \rangle \quad (3)$$

where $\langle u^2 \rangle$ is the 2nd moment of the wind at 10-m height calculated from 6-hourly winds at ¼ ˚ resolution (Hersbach et al., 2020); Sc is the Schmidt number, and 660 is the nominal Schmidt number of CO_2 at 20 ˚C. The coefficient 0.251 is determined from scaling the gas transfer-wind speed relationship to the global average the 2nd moment of the wind and the inventory of bomb ^{14}C in the ocean (Sweeney et al., 2007).

The F_{sa} (mol m^{-2} y^{-1}) are aggregated into regional or global fluxes, with the flux expressed in Tg C (10^{12} g) or Pg C (10^{15} g = Gigaton). In the terrestrial and atmospheric communities bulk fluxes are often expressed as Tg or Pg of CO_2 where 1 Tg CO_2 equals 0.27 Tg C. For RECCAP2 the recommendation is that the sea-air flux be positive if the net flux is into the ocean, while in the oceanography community, and in this manuscript, the flux into the ocean (uptake) is presented as a negative value. The differences in conventions are summarized in Table A1.

For the AOML_ET method monthly maps, or fields, of fCO_{2w} are created after a training step and using predictor variables to determine the target fCO_{2w} on monthly 1˚ by 1˚ grids. The ET ML algorithm is described in detail in Geurts et al. (2006). In short, it is based on a decision tree approach of learning much like the Random Forest approach. Its training uses a tree-based ensemble where nodes are split at random cut points using all observations to build the model.

At a 1˚ by 1˚ monthly grid spacing there are 11.28 M possible grid nodes from October 1997 through December 2020, but even for the best sampled months only a small fraction have fCO_{2w}

observations in the gridded in SOCATv2021 product. The maximum coverage is 4.3 % of all cells for August 2011. For AOML_ET, 70 % of the data are placed into a training dataset, and 30 % are reserved for the testing dataset to determine bias and uncertainty expressed as a root mean square error (RSME). Testing data include all the fCO_{2w} observations from years 2000, 2005, 2010 and 2015. Omitting data from whole years is better than randomly withholding data points for testing since this could lead to favoring test data in well sampled areas and seasons causing uncertainty to not being appropriately represented.

2.2 The Takahashi 2010 climatology

To investigate seasonal and regional differences in sea-air CO_2 fluxes between approaches a comparison is made between the AOML_ET for 2010 and the updated monthly Takahashi climatology centered on 2010 (Tak-2010) created on a native resolution on a 4˚ by 5˚ grid and subsequently sub-gridded to 1˚ resolution that is submitted to RECCAP2 (DeVries et al., 2023). The creation of Tak-2010 follows the same procedures as the previous climatology centered on year 2000 (Takahashi et al., 2009). It uses the same SOCAT dataset for pCO_{2w} as the AOML_ET analysis. In Tak-2010, the pCO_{2w} values are adjusted to 2010 by assuming that pCO_{2w} increases at a similar rate as the atmospheric increase. Therefore, for pCO_{2w} data between 1957 and 1979, 1 µatm y^{-1} was added to each pCO_{2w} observation; for 1980 through 2000, 1.5 µatm y^{-1} was added; from 2001 through 2009, 2 µatm y^{-1} was added; and between 2011-2018, 2 µatm y^{-1} was subtracted to normalize the pCO_{2w} to the virtual year of 2010. The MBL-RS XCO_{2a}, P and SST values for 2010 were used in the creation of flux maps. The interpolation in Takahashi et al. (2009) is different from the gap filling in the ML and regression approaches in that it is done by using a surface water advection scheme from a coarse resolution model (Bryan & Lewis, 1979) without predictor variables. In contrast, all ML and regression methods used in RECCAP2 the fCO_{2w} rely on interpolated and gap filling using predictor variables.

2.3 Sensitivity of sea-air CO_2 fluxes to different input variables

Several adaptations of the AOML_ET default configuration are implemented to assess sensitivity to procedures and predictor variables. The following changes are applied to the default configuration of AOML_ET that uses location, time, SST, SSS, MLD, and Chl-a: The algorithm was trained without Chl-a or without MLD; $<u^2>$ was added as a predictor; the algorithm was trained against the target variable ΔfCO_2 instead of fCO_{2w}. Using ΔfCO_2 largely eliminates the externally forced component, as fCO_{2w} closely follows atmospheric CO_2 increases in the global ocean (McKinley et al., 2020; Fay et al., 2023, submitted). Most of the adaptations did not yield meaningful differences on global scales. A notable exception is substituting the target fCO_{2w} for ΔfCO_2.

To determine the effect of data quality and quantity, a training dataset was created using only the datasets flagged A and B in SOCATv2021 that have a stated accuracy of better than 2 µatm, compared to the default dataset that includes data flagged A-D where the C and D datasets are estimated to be good to within 5 µatm (Wanninkhof et al., 2013). This decreases the total number of grid cells with available data from 309,100 to 188,873 (Figure S1) and decreases coverage in time, with no A, B data before 1990, and less data in high latitude and coastal regions (Figure S2). As the uncertainty of the observations is not explicitly incorporated into the analyses, the

differences will primarily show up in lower data count and regional coverage, with a decrease in average number of cells with observations from 2.2 % to 1.5 % using only A and B data.

For investigating the impact of other variables needed to determine fluxes beyond those used to create fCO_{2w} fields, the effect of using a different XCO_{2a} product is investigated as regional differences in XCO_{2a} can impact the fluxes (Wanninkhof et al., 2019). In the RECCAP2 protocol, XCO_{2a} values from the MBL-RS are used with samples for XCO_{2a} taken weekly at 60 sites around the globe forming the basis of this product (https://gml.noaa.gov/ccgg/about/global_means.html, Dlugokencky, 2021). These zonal averages are almost exclusively used in global CO_2 flux estimates.

In this zonally invariant MBL-RS product, the XCO_{2a} is expressed with time and latitude. To match the fCO_{2w} resolution, the XCO_{2a} data is re-gridded on a monthly 1˚ by 1˚ grid and used to calculate fCO_{2a} by:

$$fCO_{2a} = G_f(T,S)\,(P - pH_2O)\,XCO_{2a} \quad (4)$$

where P is the barometric pressure at sealevel, $G_f(T,S)$ is the fugacity correction (≈ 0.996 to 0.997 from 0 to 30 ˚C) and pH_2O is the saturation water vapor pressure at P and SST as summarized in Pierrot et al. (2009).

The default MBL-RS product is compared with XCO_{2a} over the ocean surface derived from CarbonTracker CT2019B (Jacobson et al., 2020). CT2019B provides a spatially and temporally-varying representation of XCO_{2a} throughout the atmosphere created by assimilating a wide variety of atmospheric CO_2 data in a 3-D atmospheric chemistry-transport model, TM5 (Krol et al., 2005). This CT-PBL product provides XCO_{2a} globally at 3-hourly intervals and at 3˚ longitude by 2˚ latitude spanning 2000-2020. The PBL height in TM5 is estimated from the ERA5 driving meteorology and a bulk Richardson number formulation (Jacobson and Munro, pers. com.) where the XCO_{2a} for each of the layers within the PBL is averaged. Then the 3˚ longitude by 2˚ latitude bins are regridded to a 1˚ by 1 and averaged monthly to determine the fCO_{2a} (Eqn. 4) and the flux (Eqn. 1). This output is referred to as the CT-PBL product.

The effect of different wind speed products and parameterizations have been detailed in Roobaert et al. (2018), including discussion of the rationale for normalizing the wind products and gas transfer-wind speed dependencies. Two different parameterizations are compared here that differ in their assumptions of environmental forcing as detailed in Wanninkhof et al. (2009). A quadratic with zero intercept,

$$k_{660} = 0.251 \langle u_{10}^2 \rangle \quad (5)$$

and a third-order polynomial dependency with wind with non-zero intercept, or hybrid parameterization,

$$k_{660} = 3 + 0.1 \langle u_{10} \rangle + 0.083 \langle u_{10}^2 \rangle + 0.011 \langle u_{10}^3 \rangle \quad (6)$$

are compared. The coefficient for the 2nd moment of the wind has been adjusted in Eqn. 6 from 0.064 in the original equation of Wanninkhof et al. (2009) to 0.083 to account for the different wind fields used between the original work and here. The parameterizations are shown versus wind speed in Figure 2.

3 Discussion

The variability in sea-air CO_2 fluxes is largely driven by surface water fCO_{2w} but other drivers can have an impact on the fluxes, particularly on regional scales. The salient features of the fluxes based on the fCO_{2w} obtained with the AOML_ET method, as one of the eleven pCO_2 based approaches used in RECCAP2 (DeVries et al., 2023), are compared with Tak-2010. We describe the sensitivity of the global sea-air CO_2 flux to different predictor variables and using subsets of data. Comparisons of various ML approaches have been shown in other works (e.g. Rödenbeck et al., 2015; Gregor et al., 2019; and Stammel et al., 2020) and will not be a focus within.

3.1 Global and regional trends in fluxes using the AOML_ET method

A high level summary of results of the AOML_ET method are shown in Figure 3. The annual global fluxes from 1998-2020 are shown in Figure 3a along with permutations of the method described below. Figure 3b presents a Taylor diagram of observed and predicted values. For AOML_ET a coefficient of correlation, r^2 of 0.83 was obtained, and a RMSE of 17 µatm in line with other ML and regression estimates (Gregor et al., 2019). The standard deviation, indicating the variability, is 34 µatm compared to 43 µatm for the observations.

Representative flux maps for the AOML_ET method for January and July 2010 provide a visual depiction of spatial and seasonal differences in flux density (Figure 4) with well-described features (e.g. Takahashi et al., 2009). The overall patterns and magnitude of AOML_ET fluxes are in agreement with other data-based ML, regression approaches and climatologies used in RECCAP2. There is outgassing in the tropical oceans and upwelling regions, and uptake in subtropical and subarctic areas. Seasonal progressions are seen in the subtropics that change from strong sinks in wintertime to a source in summer, primarily driven by changes in SST. A strong source in the Bering Sea is prevalent in the wintertime, contrary to other Northern high latitude regions that are wintertime sinks. This is attributed to deepening of the mixed layer in winter entraining water with high CO_2. Overall, the winter season shows greater uptake than summertime in the respective hemispheres. Globally, greatest uptake is in the December-February timeframe.

The annual global fluxes from the AOML_ET approach falls within the range of other ML methods albeit with a more negative global trend of -0.9 Pg C dec^{-1} than many of the approaches (Figure 1, Table 1). This is, in part, attributed to the low fluxes at the beginning of the time series, which combined with anthropogenic CO_2 emissions causing increasing fCO_{2a} leads a larger sea-air CO_2 disequilibrium. That is, the ΔfCO_2 becomes more negative, and thereby increases the CO_2 flux into the ocean and leads to a larger negative trend. Indeed, an inverse relationship between the flux in 1998 versus trend is observed when comparing the different ML methods (Figure 5) showing the negative feedback of low fluxes at the beginning of the record for most approaches used in RECCAP2 leading to higher trends.

Differing trends in regional fluxes are apparent in the AOML_ET fluxes over the 1998-2020 time period. Significant areas show the expected negative trends (Figure 6a) with statistical significance (Figure 6b). That is, the rising atmospheric CO_2 levels will cause greater uptake/less outgassing, and thus a negative trend in fluxes. This negative trend is prevalent in the seasonally stratified high latitude regions. Neutral and positive trends, that indicate less uptake or more outgassing over time, are apparent in mid- and low-latitude regions and can be attributed to the rise in SST and possible decrease in biological productivity (Landschützer et al., 2018). In broad brush, the trends are in agreement with observation-based regional analyses of Fay and McKinley (2013) that provide trends of fCO_{2w} instead of sea-air CO_2 fluxes shown here, recognizing that positive trends in fCO_{2w} leads to smaller negative trends in flux. Their analysis indicates that regions with a stronger trend in fCO_{2w} than expected from atmospheric increases correspond to areas with increasing SST. They also show that regions with prevailing deep (winter) mixed layers show smaller increases in fCO_{2w}, which are the regions of increasing negative flux trends in our analysis.

3.2 Comparison of AOML_ET with the Takahashi 2010 (Tak-2010)

For this comparison the fluxes derived from AOML_ET in 2010 are compared to the climatology of Takahashi centered on 2010. The fluxes determined in AOML_ET in 2010 and the Tak-2010 climatology are very similar in magnitude and pattern. For the global comparison of the AOML_ET and Tak-2010, the surface areas are normalized. That is, the global fluxes in Tak-2010 are scaled by 1.15 to account for the smaller ocean area covered. The global average sea-air CO_2 flux and monthly variability expressed as the standard deviation of the monthly values in 2010 are -2.03 ± 0.46 and -1.86 ± 0.52 Pg C for the AOML_ET and Tak-2010, respectively.

The fluxes in both products show a seasonality with greatest uptake of about 0.2 Pg C mo^{-1} from November through March and smallest uptake of about 0.1 Pg C mo^{-1} in August (Figures 7a,b). Overall, the differences in global monthly uptake between products is small at less than 0.05 to 0.1 Pg C mo^{-1}, with largest differences in February-March (Figure 7c). The tropical regions (14˚S-14˚N) are areas with persistent outgassing throughout the year in both products with Tak-2010 showing greater outgassing during the boreal spring and summer compared to AOML_ET (Figure 7). This is attributed, in part, to the fact that by nature Tak-2010 does not capture modes of interannual variability such as caused by the El Niño Southern Oscillation (ENSO). The lower outgassing within the 14˚N to 14˚S band in the boreal spring year of 2010 when El Niño conditions persisted, as shown in AOML-ET in 2010, would not be reflected in Tak-2010. The latter part of the year 2010 which experienced La Niña conditions shows very similar magnitudes of fluxes in the tropics between products (Figures 7a,b). Similarities in products include that the regions from 50˚N to 14˚N, and 50˚S to 14˚S are sinks, with wintertime for the respective hemispheres showing greater uptake for both products. The exception is that 50˚N to 14˚N has effluxes from July through September. The high latitudes (> 50˚N/S) are areas with persistent sinks with summertime showing the largest negative fluxes in line with increased biological productivity drawing down the surface water fCO_{2w} (Takahashi et al., 2009). In the seasonal ice zone (> 62 ˚S) wintertime uptake is negligible, largely because of ice cover.

Figure 7c provides a bar chart of the differences between AOML_ET in 2010 and Tak-2010 per zonal region where small differences in monthly fluxes between products are attributed to differences in the extrapolation/gap filling method applied to the fCO_{2w} values as gas transfer velocities and fCO_{2a} are the same. Of note is that the differences are zonally compensating with adjacent regions of both positive and negative differences in each month and bands partially offsetting each other. Aside from differences in the tropical region described above, there are also small differences between the AOML_ET and Tak-2010 products in the 14˚N -50˚N and 14˚S -50˚S regions. In the 14˚N-50˚N zonal band the AOML_ET product shows less uptake for much of the year except from July through September when the region outgasses for both products but with greater outgassing in Tak-2010 (Figure 7b,c). The differences between 15˚S and 50˚S largely counteract the differences to the north except from October through December when AOML_ET shows less uptake compared to Tak-2010.

The subpolar divergence zone and marginal ice zones in the Southern Hemisphere represented by the bands from 50˚S-62˚S and >62˚S are postulated to represent a CO_2 source based on calculated values of fCO_{2w} from pH sensors on profiling floats (Gray et al., 2018; Bushinsky et al., 2019). Few data exist in this region within the SOCAT database, particularly in wintertime such that the flux values reported for these regions will largely be dependent on gap filling. Both products show uptake in the summer months (November-March) and less uptake in the winter. The subpolar divergence zone in the Tak-2010 climatology shows weak outgassing while the AOML_ET shows a weak sink. Physically, a source is expected in this area due to upwelling of deep water with high CO_2 values, thus, the results here suggest that the training data for AOML_ET is insufficient to train the algorithm for this region, and that the climatology interpolation with an advection scheme provides a slightly better representation. Overall, the two very different approaches of data utilization and gap filling show reasonable agreement suggesting that different interpolation/gap filling approaches do not have a determining effect on zonal fluxes even in data sparse regions.

3.3 Sensitivity of fCO_{2w} to predictor variables and change of target variable

The different interpolation methods, and differences in the resulting fCO_{2w} and flux maps have been discussed by others (Fay et al., 2021; Gregor et al., 2019; Stamell et al., 2020 and references therein) and we limit our discussion to the AOML_ET output only. Quantitatively assessing the sensitivity of fCO_{2w} to predictor variables in the ET method is challenging due to inherent cross correlations between variables. Thus we use feature importance to assess the influence of predictor variables to construct fCO_{2w} fields (Figure 8). Location, expressed as the sum of Latitude (LAT); and vector longitudes, sine (SLON) and cosine (CLON), with a score of 0.35, has the greatest importance, in part because no bagging or clustering is performed on the fCO_{2w} data, other than the initial binning in the creation of the monthly 1˚ by 1˚ SOCAT product. This is followed by SST with a score of 0.22. This strong dependence of fCO_{2w} with SST is similar to most other gap filling techniques (Bennington et al., 2022), due to the strong physical and chemical dependency of fCO_{2w} with temperature with $\partial fCO_{2w}\ \partial T^{-1} = 0.042$ (Wanninkhof et al., 2022). Time (Julian day, JDN) is the main driver of trends due to the increasing atmospheric CO_2 levels over time. While several gap filling approaches, notably MLR interpolations, have shown weak correlation with Chl-a, Chl-a is important in construction of the AOML_ET with a score of 0.1. The other predictor variables, MLD, and SSS, each have similar scores of ≈0.1.

The impact of omitting predictor variables on global CO_2 fluxes is summarized in Figure 3a which shows AOML_ET output created without MLD and separately without Chl-a. These predictor values were selected for omission as their quality and resolution are of lower fidelity than the other predictors, particularly at the start of the record. MLD are model derived and Chl-a is a satellite ocean color product interpolated for regions and times with cloud cover. Overall, with these predictor variables omitted, no large impacts are seen in the global annual averages with all runs showing approximately the same magnitude, variability and trends, within their monthly variability of 0.3 Pg C y^{-1} (Figure 3a). Omitting Chl-a increases the annual global uptake by about 0.2 Pg C y^{-1} up to 2018 after which the global uptake decreases by 0.3 Pg C y^{-1} between 2018 and 2020 compared to the default AOML_ET configuration. Omitting MLD has a much smaller global effect with differences < 0.1 Pg C y^{-1} for the record up to 2018 after which the uptake follows the same pattern as omitting Chl-a. Adding the second moment of the wind $<u^2>$ as a predictor variable does not show any differences with the default AOML_ET, except from 2018 onward when uptake using $<u^2>$ is about 0.1 Pg C y^{-1} greater than the default.

In contrast, a large difference in the magnitude of global fluxes was observed when training with ΔfCO_2 as a target variable instead of fCO_{2w}. Resulting net sea-air CO_2 fluxes are -3 Pg C in 1998 and -4 Pg C in 2020 or approximately 2 to 1.5 Pg C y^{-1} greater uptake than the default AOML_ET version. (Figure 3a). The trend in the flux with time is less as well compared to the default configuration. The trend for the ΔfCO_2 target run from 1998-2020 is -0.55 Pg C $y^{-1}decade^{-1}$ compared to -0.9 Pg C y^{-1} $decade^{-1}$ for the default AOML_ET product. The trend using ΔfCO_2 is more in line with other ML approaches that show an average trend of -0.7 Pg C y^{-1} $decade^{-1}$ since 1998 (Table 1). The cause for the poor agreement in magnitude of the global flux combined with the lower trend using ΔfCO_2 instead of fCO_{2w} is unclear. Changes ΔfCO_2 over time are expected to be relatively small with time as on decadal timescales the fCO_{2w} closely tracks fCO_{2a} due to the relatively rapid equilibration time of surface waters with the marine boundary layer of 3-6 months. This could explain the lower trend but as noted the large flux should lead to decreasing the ΔfCO_2 over time and cause a strong feedback that would not maintain such a flux.

As shown in the Taylor diagram (Fig 3b) the different permutations do not appreciably impact the RMSE, variability (as expressed as a standard deviation of all data over the 23-year timespan) or correlation coefficient, r^2 of fCO_{2w} with all simulations showing a RMSE between 18 and 22 µatm; a r^2 between 0.83 and 0.88 and a standard deviation between 33 and 37 µatm compared to the standard deviation of data on 42 µatm (Figure 3b). The run where ΔfCO_2 is used instead of fCO_{2w} as the target variable instead of fCO_{2w} shows the best statistics with a RSME of 18 µtm, a standard deviation of 37 µatm, and r^2 of 0.88. However, as noted above the magnitude and trend of the fluxes determined in this configuration is very different from the default configuration with magnitudes not consistent with other available products (DeVries et al., 2023).

3.4 Sensitivity to data quality and quantity

The product using the AOML_ET procedure with the gridded data comprised of datasets flagged A and B with accuracy better than 2 µatm shows small differences with the default product with

slightly smaller uptake (≈ 0.2 Pg C y^{-1}) over the first part of the record and from 2013 onward (Figure 3a). Using only higher quality data lead to less gridded data points and slightly degrades statistics (Figure 3b) with an r^2 of 0.82 and RMSE of 22 µatm. Th default AOML_ET product has a r^2 of 0.87 and a RSME of 20. The A,B product also shows less variability at 33 µatm compared to 35 µatm of the default AOML_ET product for the 1998-2020 time period. The slightly reduced variability can, in part, be explained by the fact that the higher quality data is generally from the open ocean that exhibits less variability than the coastal seas. As suggested in Hauck et al. (2023), the SOCAT database contains more near-shore data in the latter part of the record with lower fCO_{2w} values and larger variability. This leads to a possible artifact in estimating trends and variability using the full SOCAT dataset. A more thorough analysis is required to separate the impacts of a using a subset of higher quality data versus the resulting reduced number of observations. In particular data denial approaches are a powerful means of investigation.

3.5 Sensitivity to fCO_{2a}

Sea-air CO_2 fluxes are very sensitive to the magnitude of the ΔfCO_2 (=fCO_{2w}-fCO_{2a}). A bias in ΔfCO_2 of 1 µatm globally will change the global annual sea-air CO_2 flux by ≈ 0.2 Pg C. The fCO_{2a} are often measured in conjunction with fCO_{2w}, but fluxes are commonly derived using an independent XCO_{2a} that is zonally averaged, like the MBL-RS. However, the zonal homogeneity in XCO_{2a} is not reflected in fCO_{2a} (Eqn. 4) with systematic regional differences in barometric pressure (P) and saturation water vapor pressure (pH_2O). These can cause zonal differences up to ≈16 µatm in fCO_{2a} even with constant XCO_{2a} (Figure 9). The P and pH_2O will both affect the fCO_{2w} and fCO_{2a} in a similar fashion such that errors in P and pH_2O will not have a large impact on ΔfCO_2 as long as the same P and SST products are used to calculate both fCO_{2w} and fCO_{2a}. Variability in fCO_{2w} in the open ocean is up to 10 times larger than fCO_{2a}. However, systematic differences in fCO_{2a} can be of importance due to the small global sea-air disequilibrium of ≈ -6 µatm (Figure 10) driving the fluxes.

During fall and winter months, air flowing off continents generally has higher CO_2 due to fossil fuel burning and net ecosystem respiration on land. This leads to higher XCO_{2a} over many coastal seas and larger influxes/lower effluxes, particularly along the heavily industrialized eastern continental boundaries in the Northern Hemisphere due to the prevailing westerly winds at those latitudes. During spring and summer, however, carbon uptake on land due to terrestrial photosynthesis can lead to negative zonal anomalies in XCO_{2a} which causes decreased ocean uptake, especially in coastal regions. Northcott et al. (2019) showed from extrapolating nearshore observations that the higher PBL XCO_2 could enhance global ocean CO_2 uptake by 1 %.

The impact of higher XCO_{2a} in coastal regions can be discerned by using the spatially resolved CT-PBL product compared to the zonally averaged MBL-RS product. Of note is that this effect will be quantitatively similar for fluxes derived for all the different ML and interpolation approaches. The difference in CT-PBL product versus the MBL-RS product on global scales is small because the global averages of XCO_{2a} between the MBL-RS and CT-PBL products are similar. The global monthly ocean sink differences using the CT-PBL compared to the MBL-RS XCO_2 from 2000-2020 are -0.02 ± 0.05 Pg C with the CT-PBL product showing slightly greater

fluxes into the ocean on average. No appreciable year-to-year differences are observed. The regional differences can be large with this change, particularly in the winter months. The largest differences are off the East Coasts of North America and Asia. Figure 11 shows the differences in the 30-35˚N latitude band for 2010 between fluxes derived from the MBL-RS and CT-PBL as a representative example. The entire latitude band shows the characteristic seasonal pattern for the subtropics with a strong sink in winter and weak source in summer with an annual average for 2010 of -0.61 mol m^{-2} y^{-1} for the MBL-RS product and -0.66 mol m^{-2} y^{-1} for the CT-PBL product. The Mid Atlantic Bight (MAB) off the coast of the USA (30-35˚N, 75-70˚W) and Yellow Sea (30-35˚N, 120-125˚W) show wintertime enhancement of uptake by 6 and 21 %, respectively in agreement with a similar exercise performed by Palter et al. (2023, accepted GRL). The differences in spring and summer are smaller with the MAB showing a slightly decreased influx during May for the CT-PBL attributed to XCO_{2a} drawdown on land due to the springtime increase in terrestrial biological productivity.

3.6 Sensitivity to the gas transfer velocity

Different gas transfer velocity formulations and wind speed products can impact the global flux estimates with past studies indicating that this is a primary source of uncertainty in global flux estimates (Woolf et al., 2019). The impact of time averaging and the effect of different wind fields has been investigated (Wanninkhof et al., 2002; Roobaert et al., 2018; and Gregor et al., 2019) but conical quadratic wind speed relationships to parameterize gas transfer are used in most flux estimates, including those in RECCAP2 (DeVries et al., 2023) and the GCB (Friedlingstein et al., 2022). A common procedure is to normalized the coefficient in the relationship (Eqn. 5) to a global average wind and gas transfer velocity value (Fay et al., 2021). Less emphasis has been placed on different functionalities of parameterizations (Wanninkhof et al., 2009). The different functionalities are of increasing importance with improved high resolution wind speeds and ΔfCO_2 mapped products such that the variability of ΔfCO_2 and $<u^2>$ are better represented. Two gas exchange wind parameterizations are compared which are both in accord with the global ocean bomb ^{14}C inventories. The default parametrization is depicted in Eqn. 5, and the polynomial expression is shown in Eqn. 6 that is sometimes listed as a hybrid dependency. The rationale of the two parameterizations based on the controls of gas transfer at the interface is described in Wanninkhof et al. (2009).

The results show negligible global flux differences of 0.003± 0.011 Pg C between a quadratic dependency with wind, (Eq. 5) and hybrid expression (Eqn. 6). The uncertainly is captured in the standard deviation of annual differences from 1998-2020. While the results are the same on global scale, the different gas transfer parameterizations show significant differences in regional patterns of fluxes. Figure 12 shows maps of differences in fluxes between the quadratic and hybrid relationships for January and July 2010. The hybrid expression shows larger fluxes in select tropical and other low wind, doldrum, regions with winds persistently less than 5 m s^{-1}. These are areas with mostly effluxes of CO_2. The effect of lower winds in the Northern Hemisphere tropical and subtropical regions during July is apparent compared to the windier times in the boreal winter (Figure 12b). Only few regions show larger fluxes at high winds (≈> 13 m s^{-1}) with the hybrid expression. Notably, parts of the Bering Sea in January 2010 show higher fluxes with the hybrid parameterization and since the region has positive ΔfCO_2, the hybrid parameterization leads to higher effluxes. Mid-latitude regions with prevailing winds

between 5 and 13 m s^{-1} will have lower k_{660} with a hybrid parameterization and correspondingly show lower fluxes.

4 Conclusions

The AOML_ET method described here is one of the observation-based fCO_2 approaches used in RECCAP2 to interpolate fCO_{2w} observations into uniform fields, and determine global sea-air CO_2 fluxes on monthly 1˚ by 1˚ resolution. The ET approach may suffer from spurious results in under sampled regions compared to other ML mapping approaches. However its merits include transparency and computational efficiency. The average flux of the AOML_ET method falls in line with other approaches but with a greater long term trend from 1998-2000 and slightly less interannual variability than other ML methods. The results for the year 2010 compare favorably in terms of both the magnitude of the flux and seasonal and regional variability with the Takahashi climatology centered on 2010. The analysis of using a different subset of the SOCAT database based on quality criteria shows broad similarities but less variability with the higher quality observation subset, likely because the high quality-only dataset is distributed more heavily in the open ocean. Therefore, the impact of higher quality data cannot be clearly discerned in this exercise as use of only higher quality data corresponds to lower data density which also may lead to lower variability in general. The changes in RMSE and r^2 for the different permutations of predictor and target values summarized in Figure 3b show no appreciable differences in flux estimates on global scales, but differences show up in regional patterns. The regional differences often are compensation leading to the good correspondence on global scales. This agrees with other analyses (e.g. Gregor et al., 2019) who show that that the different ML approaches yield similar global estimates. While agreement is encouraging, a caveat is that the same gridded fCO_{2w} dataset is used such that the true uncertainty in fluxes is likely underestimated. Similar predictors are used in all ML approaches and uncertainty and biases in predictor values are often not incorporated into the uncertainty estimates. Largest differences in ML approaches are apparent in the trends and are correlated with the magnitude of fluxes at the beginning of the record, which in this analysis is 1998.

Acknowledgments

We acknowledge the Global Carbon Project, which is responsible for the Global Carbon Budget and thank the ocean fCO_2-mapping groups for producing and making available their fCO_2-product output which are used in Figure 1. The AOML_ET product was developed as contribution the RECCAP2 effort. We appreciate the input of Andy Jacobson NOAA/GML, CIRES for providing the CT-PBL boundary layer XCO_2 product and reviewing the section of this manuscript utilizing the product. Observations from over 100 investigators worldwide are collated in SOCAT that are the observational basis for this work. The many researchers and funding agencies responsible for the collection of data and quality control are thanked for their contributions to SOCAT. We thank Leticia Barbero (CIMAS/AOML) for internal review. The NOAA office of Oceanic and Atmospheric Research is acknowledged for financial support, in particular the Global Ocean Monitoring and Observations (fund reference 100007298)

Open Research

The AOML_ET results (1998-2018) and Takahashi 2010 climatology based on fCO_{2w} data from 1985-2018 can be found as part of the RECCAP2 holdings at: Müller, J.D. https://doi.org/10.5281/zenodo.7990823, Zenodo. The fluxes of the AOML_ET approach with different input variables are stored at NCEI. [links provided at acceptance]

References

Bakker, D. C. E., Pfeil, B., Landa, C. S., Metzl, N., O'Brien, K. M., Olsen, A., et al. (2016). A multi-decade record of high-quality fCO_2 data in version 3 of the Surface Ocean CO_2 Atlas (SOCAT). *Earth Syst. Sci. Data 8*, 383-413. http://www.earth-syst-sci-data.net/8/383/2016/

Bennington, V., Galjanic, T., & McKinley, G. A. (2022). Explicit Physical Knowledge in Machine Learning for Ocean Carbon Flux Reconstruction: The pCO_2-Residual Method. *Journal of Advances in Modeling Earth Systems, 14*(10), https://doi.org/10.1029/2021MS002960.

Bryan, K., & Lewis, L. J. (1979). A water mass model of the World Ocean. *Journal of Geophysical Research: Oceans, 84*(C5), 2503-2517. https://doi.org/10.1029/JC084iC05p02503.

Bushinsky, S. M., Landschützer, P., Rödenbeck, C., Gray, A. R., Baker, D., Mazloff, M. R., et al. (2019). Reassessing Southern Ocean air-sea CO_2 flux estimates with the addition of biogeochemical float observations. *Global Biogeochemical Cycles, 33*(11), 1370-1388. https://agupubs.onlinelibrary.wiley.com/doi/abs/10.1029/2019GB006176

Chau, T. T. T., Gehlen, M., & Chevallier, F. (2022). A seamless ensemble-based reconstruction of surface ocean pCO2 and air–sea CO2 fluxes over the global coastal and open oceans. *Biogeosciences, 19*(4), 1087-1109. https://bg.copernicus.org/articles/19/1087/2022/

DeVries, T., Yamamoto, K., Wanninkhof, R., Gruber, N., Hauck, J., Müller, J. D., et al. (2023). Magnitude, trends, and variability of the global ocean carbon sink from 1985-2018. *Global Biogeochemical Cycles*, e2023GB007780. https://doi.org/10.1029/2023GB007780

Dlugokencky, E.J., Thoning, K.W., Lan, X. & Tans, P.P. (2021). NOAA Greenhouse Gas Reference from Atmospheric Carbon Dioxide Dry Air Mole Fractions from the NOAA GML Carbon Cycle Cooperative Global Air Sampling Network.
Data Path: https://gml.noaa.gov/aftp/data/trace_gases/co2/flask/surface/.

Doney, S. C., Busch, D. S., Cooley, S. R., & Kroeker, K. J. (2020). The impacts of ocean acidification on marine ecosystems and reliant human communities. *Annual Review of Environment and Resources, 45*(1), 83-112. https://doi.org/10.1146/annurev-environ-012320-083019

Fay, A. R., & McKinley, G. A. (2013). Global trends in surface ocean pCO_2 from in situ data. *Global Biogeochemical Cycles, 27*(2), 541-557. https://doi.org/10.1002/gbc.20051

Fay, A. R., & McKinley, G. A. (2014). Global open-ocean biomes: mean and temporal variability. *Earth Syst. Sci. Data, 6*(2), 273-284. http://www.earth-syst-sci-data.net/6/273/2014/

Fay, A. R., Gregor, L., Landschützer, P., McKinley, G. A., Gruber, N., Gehlen, M., et al. (2021). SeaFlux: harmonization of air–sea CO2 fluxes from surface pCO2 data products using a standardized approach. *Earth Syst. Sci. Data, 13*(10), 4693-4710. https://essd.copernicus.org/articles/13/4693/2021/

Fay, A. R., Munro, D. R., McKinley, G., Pierrot, D., Sutherland, S., Sweeney, C., & Wanninkhof, R. (2023). Updated climatological mean delta fCO_2 and net sea–air CO_2 flux over the global open ocean regions. *Earth System Science Data, submitted*.

Friedlingstein, P., Jones, M. W., O'Sullivan, M., Andrew, R. M., Bakker, D. C. E., Hauck, J., et al. (2022). Global Carbon Budget 2021. *Earth System Science. Data, 14*(4), 1917-2005. https://essd.copernicus.org/articles/14/1917/2022/

Gregor, L., Lebehot, A. D., Kok, S., & Scheel Monteiro, P. M. (2019). A comparative assessment of the uncertainties of global surface ocean CO2 estimates using a machine-learning ensemble (CSIR-ML6 version 2019a) – have we hit the wall? *Geosci. Model Dev., 12*(12), 5113-5136. https://gmd.copernicus.org/articles/12/5113/2019/

Gregor, L., & Gruber, N. (2021). OceanSODA-ETHZ: a global gridded data set of the surface ocean carbonate system for seasonal to decadal studies of ocean acidification. *Earth Syst. Sci. Data, 13*(2), 777-808. https://essd.copernicus.org/articles/13/777/2021/

Geurts, P., Ernst, D., & Wehenkel, L. (2006). Extremely randomized trees. *Machine Learning, 63*(1), 3-42. https://doi.org/10.1007/s10994-006-6226-1

Gray, A. R., Johnson, K. S., Bushinsky, S. M., Riser, S. C., Russell, J. L., Talley, L. D., et al. (2018). Autonomous biogeochemical floats detect significant carbon dioxide outgassing in the high-latitude Southern Ocean. *Geophys. Res. Let.* http://dx.doi.org/10.1029/2018GL078013

Hauck, J., C. Nissen, P. Landschützer, C. Rödenbeck, S. Bushinsky, and A. Olsen (2023), Sparse observations induce large biases in estimates of the global ocean CO_2 sink: an ocean model subsampling experiment, *Philosophical Transactions of the Royal Society A: Mathematical, Physical and Engineering Sciences*, *381*(2249), 20220063, doi:10.1098/rsta.2022.0063.

Hersbach, H., Bell, B., Berrisford, P., Hirahara, S., Horányi, A., Muñoz-Sabater, J., et al. (2020). The ERA5 global reanalysis. *Quarterly Journal of the Royal Meteorological Society*, *146*(730), 1999-2049. https://doi.org/10.1002/qj.3803.

IPCC, 2018: Annex I: Glossary [Matthews, J.B.R. (ed.)]. In: *Global Warming of 1.5°C. An IPCC Special Report on the impacts of global warming of 1.5°C above pre-industrial levels and related global greenhouse gas emission pathways, in the context of strengthening the global response to the threat of climate change, sustainable development, and efforts to eradicate poverty* [Masson-Delmotte, V., P. Zhai, H.-O. Pörtner, D. Roberts, J. Skea, P.R. Shukla, A. Pirani, W. Moufouma-Okia, C. Péan, R. Pidcock, S. Connors, J.B.R. Matthews, Y. Chen, X. Zhou, M.I. Gomis, E. Lonnoy, T. Maycock, M. Tignor, and T. Waterfield (eds.)]. Cambridge

University Press, Cambridge, UK and New York, NY, USA, pp. 541-562, https://doi.org/10.1017/9781009157940.008.

Jacobson, A. R., et al. (2020), CarbonTracker CT2019B, edited, NOAA Global Monitoring Laboratory, https://doi.org/10.25925/20201008.

Krol, M., Houweling, S., Bregman, B., van den Broek, M., Segers, A., van Velthoven, P., et al. (2005). The two-way nested global chemistry-transport zoom model TM5: algorithm and applications. *Atmos. Chem. Phys., 5*(2), 417-432. https://acp.copernicus.org/articles/5/417/2005/.

Landschützer, P., Gruber, N., Bakker, D. C. E., Schuster, U., Nakaoka, S., Payne, M. R., et al. (2013). A neural network-based estimate of the seasonal to inter-annual variability of the Atlantic Ocean carbon sink. *Biogeosciences, 10*(11), 7793-7815. http://www.biogeosciences.net/10/7793/2013/

Landschützer, P., Gruber, N., & Bakker, D. C. E. (2016). Decadal variations and trends of the global ocean carbon sink. *Global Biogeochemical Cycles, 30*(10), 1396-1417. https://doi.org/10.1002/2015GB005359.

Landschützer, P., Gruber, N., Bakker, D. C. E., Stemmler, I., & Six, K. D. (2018). Strengthening seasonal marine CO_2 variations due to increasing atmospheric CO_2. *Nature Climate Change*. https://doi.org/10.1038/s41558-017-0057-x

Li, Z., Adamec, D., Takahashi, T., & Sutherland, S. C. (2005). Global autocorrelation scales of the partial pressure of oceanic CO_2. *Journal of Geophysical Research: Oceans, 110*(C8). https://doi.org/10.1029/2004JC002723.

Lida, Y., Takatani, Y., Kojima, A., & Ishii, M. (2021). Global trends of ocean CO_2 sink and ocean acidification: an observation-based reconstruction of surface ocean inorganic carbon variables. *J. Oceanogr., 77*, 323-358.

Magnan, A. K., Colombier, M., Bille, R., Joos, F., Hoegh-Guldberg, O., Portner, H.-O., et al. (2016). Implications of the Paris agreement for the ocean. *Nature Clim. Change, advance online publication*. Commentary. http://dx.doi.org/10.1038/nclimate3038

McKinley, G. A., Fay, A. R., Eddebbar, Y. A., Gloege, L., & Lovenduski, N. S. (2020). External forcing explains recent decadal variability of the ocean carbon sink. *AGU Advances, 1*(2), e2019AV000149. https://doi.org/10.1029/2019AV000149.

Müller, J. D. (2023). RECCAP2-ocean data collection [Version V1]. https://doi.org/10.5281/zenodo.7990823, Zenodo

Northcott, D., Sevadjian, J., Sancho-Gallegos, D. A., Wahl, C., Friederich, J., & Chavez, F. P. (2019). Impacts of urban carbon dioxide emissions on sea-air flux and ocean acidification in nearshore waters. *PLoS ONE, 14*(3), e0214403. https://doi.org/10.1371/journal.pone.0214403

Palter, J. B., Nickford, S., & Mu, L. (2023). Ocean carbon dioxide uptake in the tailpipe of industrialized continents. *Geophysical Research Letters, accepted*.

Pierrot, D., Neil, C., Sullivan, K., Castle, R., Wanninkhof, R., Lueger, H., et al. (2009). Recommendations for autonomous underway pCO_2 measuring systems and data reduction routines. *Deep -Sea Res II, 56*, 512-522.

Rödenbeck, C., D. C. E. Bakker, N. Gruber, Y. Iida, A. R. Jacobson, S. Jones, et al. (2015). Data-based estimates of the ocean carbon sink variability –first results of the Surface Ocean pCO_2 Mapping intercomparison (SOCOM). *Biogeosciences, 12*, 7251-7278.

Rödenbeck, C., DeVries, T., Hauck, J., Le Quéré, C., & Keeling, R. F. (2022). Data-based estimates of interannual sea–air CO_2 flux variations 1957–2020 and their relation to environmental drivers. *Biogeosciences, 19*(10), 2627-2652. https://bg.copernicus.org/articles/19/2627/2022/

Roobaert, A., Laruelle, G. G., Landschützer, P., & Regnier, P. (2018). Uncertainty in the global oceanic CO_2 uptake induced by wind forcing: quantification and spatial analysis. *Biogeosciences, 15*(6), 1701-1720. https://www.biogeosciences.net/15/1701/2018/

Stamell, J., Rustagi, R. R., Gloege, L., & McKinley, G. A. (2020). Strengths and weaknesses of three Machine Learning methods for pCO_2 interpolation. *Geosci. Model Dev. Discuss., 2020*, 1-25. https://gmd.copernicus.org/preprints/gmd-2020-311/

Sweeney, C., Gloor, E., Jacobson, A. R., Key, R. M., McKinley, G., Sarmiento, J. L., & Wanninkhof, R. (2007). Constraining global air-sea gas exchange for CO_2 with recent bomb C-14 measurements. *Global Biogeochem. Cycles, 21*(2), GB2015.

Takahashi, T., Feely, R. A., Weiss, R., Wanninkhof, R., Chipman, D. W., Sutherland, S. C., & Takahashi, T. T. (1997). Global air-sea flux of CO_2: An estimate based on measurements of sea-air pCO_2 difference. *Proc. Natl. Acad. Sci. USA, 94*, 8292-8299.

Takahashi, T., Sutherland, S. C., Wanninkhof, R., Sweeney, C., Feely, R. A., Chipman, D. W., et al. (2009). Climatological mean and decadal change in surface ocean pCO_2, and net sea-air CO_2 flux over the global oceans. *Deep -Sea Res II, 2009*, 554-577.

Telszewski, M., Chazottes, A., Schuster, U., Watson, A. J., Moulin, C., Bakker, D. C. E., et al. (2009). Estimating the monthly pCO_2 distribution in the North Atlantic using a self-organizing neural network. *Biogeosciences, 6*, 1405-1421.

Wanninkhof, R., Doney, S. C., Takahashi, T., & McGillis, W. R. (2002). The effect of using time-averaged winds on regional air-sea CO_2 fluxes. In M. Donelan, W. Drennan, E. Saltzman, & R. Wanninkhof (Eds.), *Gas Transfer at Water Surfaces* .Geophysical Monograph 127, pp. 351-357. Washington, DC: AGU, Geophysical Monograph 127.

Wanninkhof, R., Asher, W. E., Ho, D. T., Sweeney, C. S., & McGillis, W. R. (2009). Advances in quantifying air-sea gas exchange and environmental forcing. *Annual Reviews Mar. Science, 1*, 213-244,.

Wanninkhof, R., Park, G.-H., Chelton, D., & Resien, C. (2011). Impact of small-scale variability on air-sea CO_2 fluxes. In S. Komori, W. McGillis, & R. Kurose (Eds.), *Gas transfer at water surfaces 2010* (pp. 431-444). Kyoto: Kyoto University Press.

Wanninkhof, R., Bakker, D., Bates, N., Olsen, A., & Steinhoff, T. (2013). Incorporation of alternative sensors in the SOCAT database and adjustments to dataset quality control flags. Retrieved from Oak Ridge, Tennessee: https://doi.org/10.3334/CDIAC/OTG.SOCAT_ADQCF

Wanninkhof, R. (2014), Relationship between wind speed and gas exchange over the ocean revisited, *Limnol and Oceanogr: Methods, 12*, 351-362, https://doi.org/10.4319/lom.2014.12.351.

Wanninkhof, R., Pickers, P. A., Omar, A. M., Sutton, A., Murata, A., Olsen, A., et al. (2019). A Surface Ocean CO_2 Reference Network, SOCONET and Associated Marine Boundary Layer CO_2 Measurements. *Frontiers in Marine Science, 6*, 400. 10.3389/fmars.2019.00400. https://www.frontiersin.org/article/10.3389/fmars.2019.00400

Wanninkhof, R., Pierrot, D., Sullivan, K., Mears, P., & Barbero, L. (2022). Comparison of discrete and underway CO_2 measurements: Inferences on the temperature dependence of the fugacity of CO_2 in seawater. *Marine Chemistry, 247*, 104178. https://www.sciencedirect.com/science/article/pii/S0304420322000950

Watson, A. J., Schuster, U., Shutler, J. D., Holding, T., Ashton, I. G. C., Landschützer, P., et al. (2020). Revised estimates of ocean-atmosphere CO_2 flux are consistent with ocean carbon inventory. *Nature Communications, 11*(1), 4422. https://doi.org/10.1038/s41467-020-18203-3

Weiss, R. F., & Price, B. A. (1980). Nitrous oxide solubility in water and seawater. *Mar. Chem., 8*, 347-359. ,https://doi.org/10.1016/0304-4203(80)90024-9.

Zeng, J., Nojiri, Y., Landschützer, P., Telszewski, M., & Nakaoka, S. (2014). A Global Surface Ocean fCO2 Climatology Based on a Feed-Forward Neural Network. *Journal of Atmospheric and Oceanic Technology, 31*, 1838-1849. doi:https://doi.org/10.1175/JTECH-D-13-00137.1.

Appendix:

The default configurations of the ET sea-air CO_2 flux product, AOML_EXTRAT, submitted to RECCAP2 , was produced to meet the RECCAP2 requirements and nomenclature. The output provided for RECCAP2 are pCO_2 values on a 1˚ by 1˚ monthly grid. The details of the predictor and target variables, units, and nomenclature as prescribed by RECCAP2, and those used AOML_EXTRAT_1998-2020 are provided in Table A1. If the AOML_ET parameters are different than specified in RECCAP2 they are added in italics.

Appendix Table A1

Creation of pCO_2 maps

Variables[1]	abbrev.	unit	Source/notes
Training set			
Partial pressure of CO_2	$spCO_2$	µatm	monthly gridded data SOCATv2020[2]
Fugacity of CO_2	fCO_{2w}	µatm	SOCAT v2020[3] .
Sea surface temperature	SST	˚C	gridded data SOCAT v2020
Sea surface salinity	SSS		gridded data SOCAT v2020
Mixed layer depth	MLD		HYCOM model[4]
Julian day	JDN	mo	month since Oct. 1997
Latitude	LAT	degree	
Longitude	SLON	degree	vector longitude (SIN)
Longitude	CLON	degree	vector longitude (COS)
Chlorophyll-a	Chl-a	log (mg/l)	oceancolor.gsfc.nasa.gov
Dependent variable/ Target			
Partial pressure of CO_2	$spCO_2$	µatm	for surface water
Fugacity of CO_2	fCO_{2w}	µatm	for surface water
Predictor/Interpolation variable			
Sea surface temperature	STT	˚C	NOAA OISST
Sea surface salinity	SSS		HYCOM
Mixed layer depth	MLD	m	HYCOM
Chlorophyll-a	Chl-a	log (mg/l)	oceancolor.gsfc.nasa.gov[5]
Julian day	JDN	mo	month since Oct. 1997
Latitude	Lat		
Longitude	SLON		vector longitude (SIN)
Longitude	CLON		vector longitude (COS)

Determination of flux maps

Dependent variable			
Sea-air CO_2 flux density	F_{sa}	mol m^{-2} s^{-1}	$F_{sa} = k\ K_0\ (1-f_{ice})\ (pCO_{2atm}-spCO_2)$
Sea-air CO_2 flux density	F_{sa}	mol m^{-2} y^{-1}	$F_{sa} = k\ K_0\ (1-f_{ice})\ (fCO_{2w}-fCO2_a)$
Sea-air piston velocity K_w	m s^{-1}		Wanninkhof (1992, 2014)
Gas transfer velocity	k	cm hr^{-1}	Wanninkhof (2014) .
Schmidt number	Sc		Wanninkhof (2014)
Second moment wind	$<u^2>$	m^2s^{-2}	ERA5 wind[6]
Solubility	alpha	mol $kg^{-1}atm^{-1}$	Weiss and Price (1980)
Solubility	K_0	mol $l^{-1}atm^{-1}$	Weiss and Price (1980)
Ice cover	f_{ice}	fraction	NOAA OISST[7]
Water partial pressure	$spCO_2$	µatm	SOCAT
Water fugacity of CO_2	fCO_2	µatm	SOCATV2020
Air partial pressure	pCO_{2atm}[8]	µatm	zonal mo. average xCO_2 MBL-RS
Air fugacity of CO_2	fCO_{2a}[9]	µatm	zonal mo. average xCO_2 MBL-RS
Partial pres. difference	ΔpCO_2	µatm	pCO_{2atm}- $spCO_2$
Air-water fugacity difference	ΔfCO_2	µatm	fCO_{2w}-fCO_{2a}

Global Flux	fgco2_glob	Pg C y^{-1}	Efflux negative in RECCAP2
Flux	F	Pg C y^{-1}	Efflux positive

1. Extra Trees (ET) regressors used to estimate the $spCO_2/fCO_{2w}$ values are: date, location, sea surface temperature, sea surface salinity, mixed-layer depth, and chlorophyll concentration.
2. SOCAT data are converted from fCO_2 to pCO_2 to meet the RECCAP2 submission criteria. These are gridded products based on the monthly 1˚ by 1˚ gridded SOCATv2020 data holdings using datasets with QC flags of A through D, and SOCAT data points flagged with WOCE flag values of 2. See, https://www.ncei.noaa.gov/data/oceans/ncei/ocads/data/0210711/ SOCATv2020_Gridded_Dat/ SOCATv2020_tracks_gridded_monthly.nc. The submission to RECCAP2 for the time period October 1997- December 2018 uses data from SOCATv2020 while the analysis in this paper uses SOCATv2021 and covers the time period October 1997- December 2020.
3. Two Different SOCATv2020 products are used in our analyses, the first is the default (see footnote 2) and a product using only datasets labeled A and B with accuracies better than 2 µatm (compared to 5 µatm in the full dataset).
4. Mixed layer depth is based on a criteria of 0.03 change in density and provided in http://orca.science.oregonstate.edu/2160.by.4320.monthly.hdf.mld030.hycom.php
5. Chl-a are from the NASA Ocean color Monthly Fields from SeaWiFS, and AQUA/TERRA-MODIS from: https://oceancolor.gsfc.nasa.gov/.
6. From https://www.ecmwf.int/en/forecasts/datasets/reanalysis-datasets/era5 where the 6-hourly winds are aggregated on the monthly 1˚ by 1˚ grid to produce the second and third moments of the wind, $<u^2>$, and $<u^3>$.
7. From ftp://ftp.cdc.noaa.gov/Datasets/noaa.oisst.v2/icec.mnmean.nc following the approach of Takahashi et al, (2005) where k is scaled by (1-f) where f is the fraction of sea-ice covering the monthly 1˚ x 1˚ grid.
8. $pCO_{2atm} = P\ (1\text{-}pH_2O)\ XCO_{2a}$ where XCO_{2a} is the interpolated MBL-RS product from NOAA/GML: https://www.esrl.noaa.gov/gmd/ccgg/mbl/mbl.html#ghg_product.
9. $fCO_{2a} = Gf(T,S)\ (P\ -pH_2O)\ XCO_{2a}$ where, Gf(T,S) is the fugacity correction and pH_2O is the water vapor correction as summarized in Pierrot et al. (2009). P is the barometric pressure.

Figures

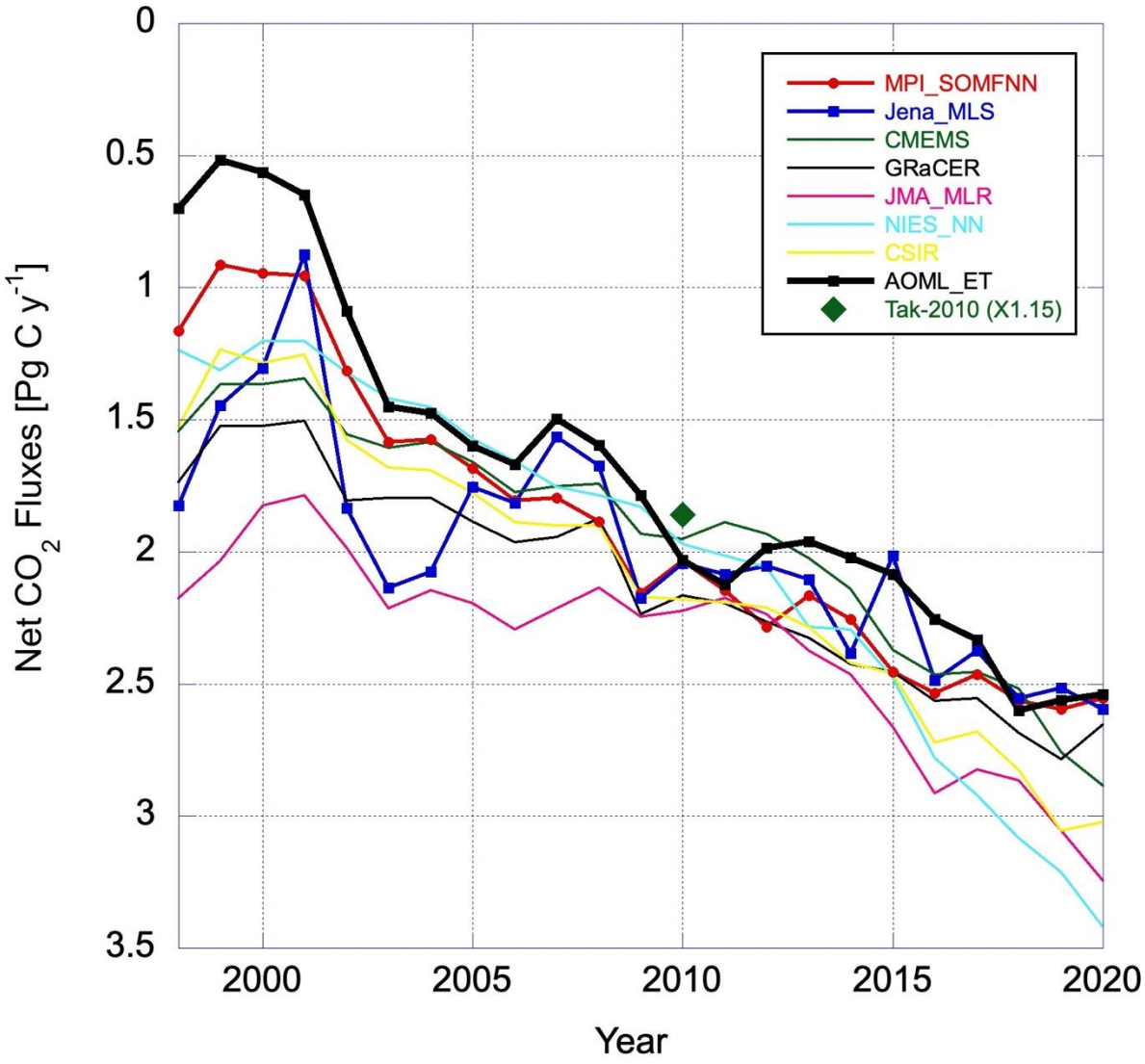

Figure 1. Global net air-sea CO_2 fluxes from 1998-2020 determined with a variety of ML and regression approaches. Data are from https://globalcarbonbudgetdata.org/latest-data.html [Global_Carbon_Budget_2022v1.0.xlsx] [0.65 Pg C is subtracted to get the net air-sea CO_2 flux]. For references of the methods see caption Table 1.

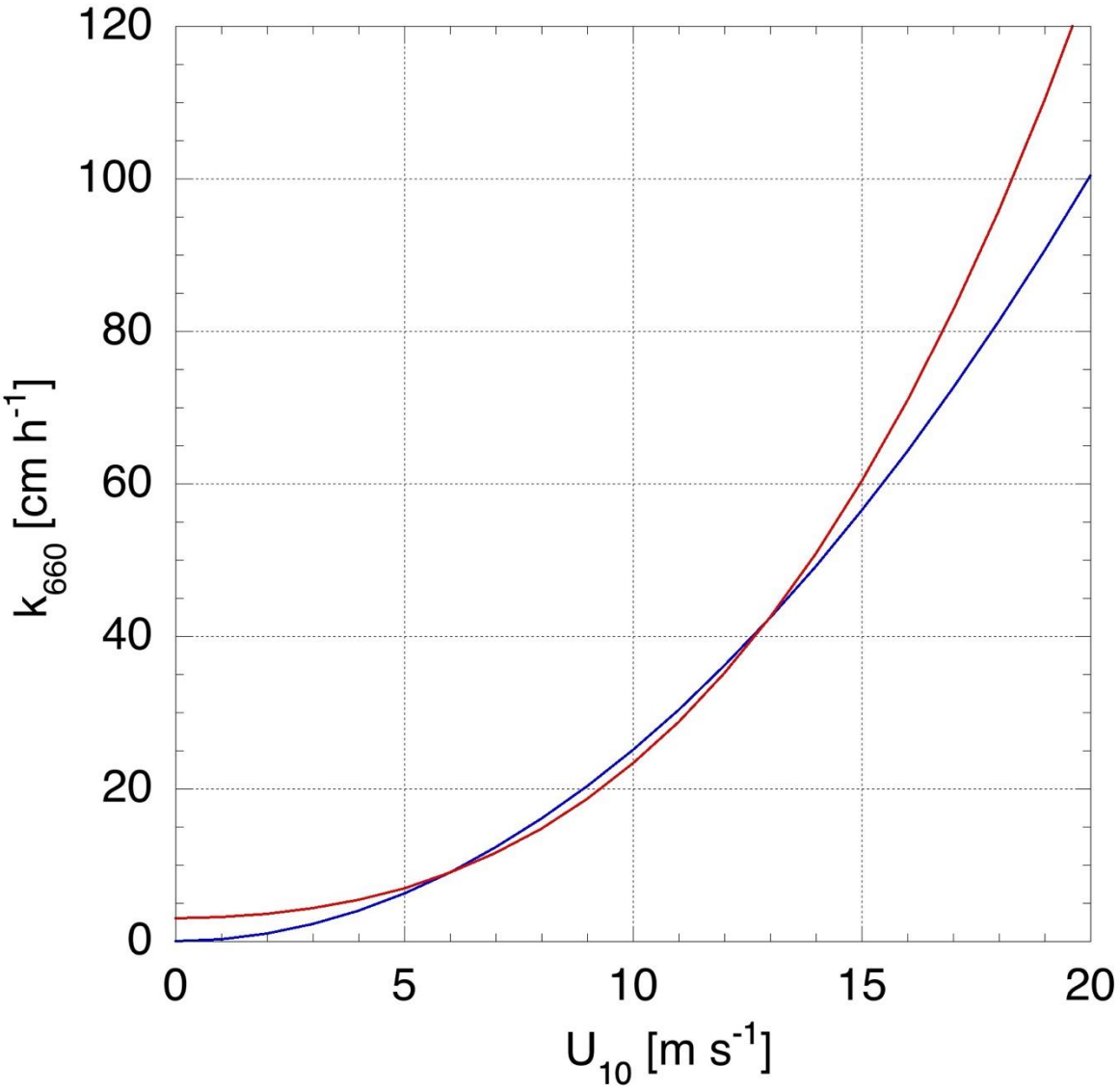

977
978 Figure 2. The canonical dependence of gas transfer with the square of square the windspeed,
979 k_{660}= 0.251 $\langle u^2 \rangle$ (blue line) and a hybrid dependence k_{660}= 3 + 0.1 $\langle u \rangle$ + 0.083 $\langle u^2 \rangle$ +
980 0.011 $\langle u^3 \rangle$ meeting the same global uptake of bomb ^{14}C constraint. For wind between 5
981 and 13 m s^{-1} the wind speed squared relationship will yield larger gas transfer
982 velocities, outside this range the hybrid dependence yields greater fluxes.
983

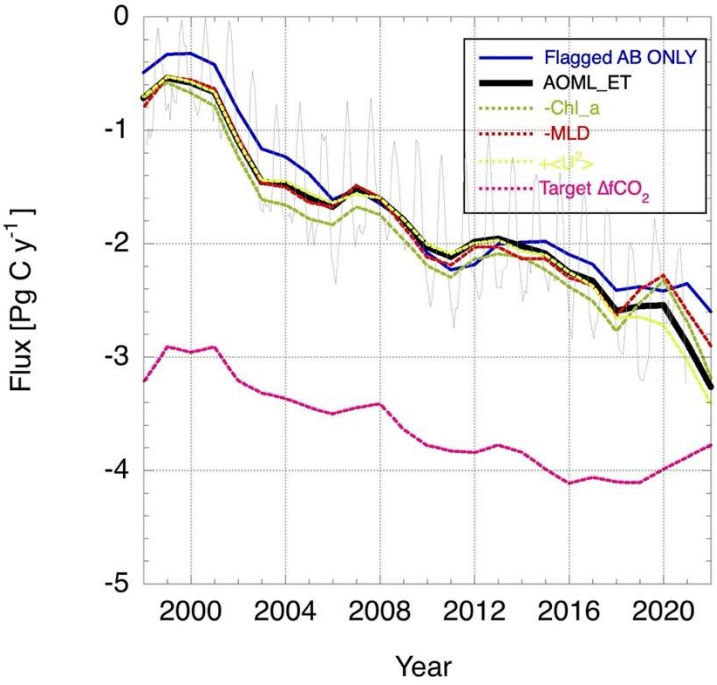

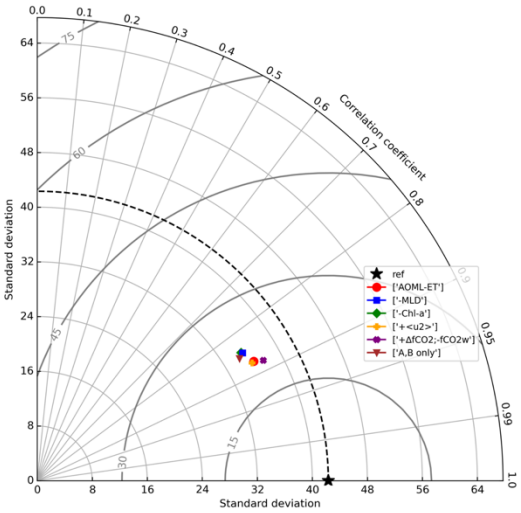

Figure 3. (a) Global net air-sea CO_2 fluxes from 1998-2020 using different predictor and target variables for the AOML_ET method. Black line: default AOML_ET; blue line: SOCAT data flagged A or B < 2µatm only; green dashed line: omitting Chl-a as predictor; red dashed line: omitting MLD as predictor; yellow dashed line: including $<u^2>$ as predictor; and pink dashed line: using ΔfCO_2 instead of fCO_{2w} as target. The thin gray line shows the monthly variation in flux for AOML_ET (b) a Taylor diagram of the AOML_ET values for the permutations listed in a.

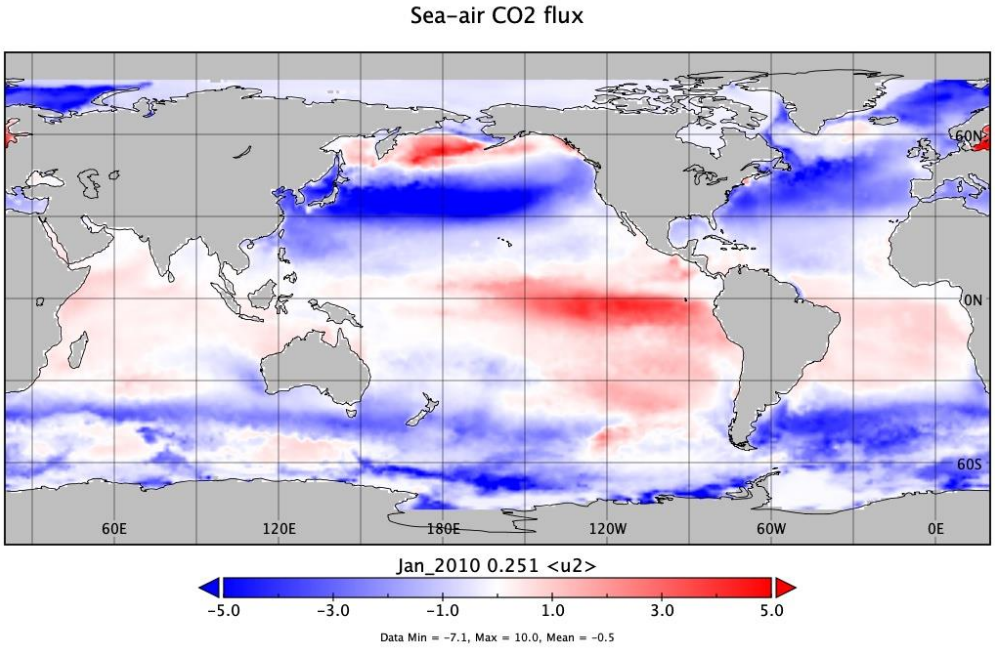

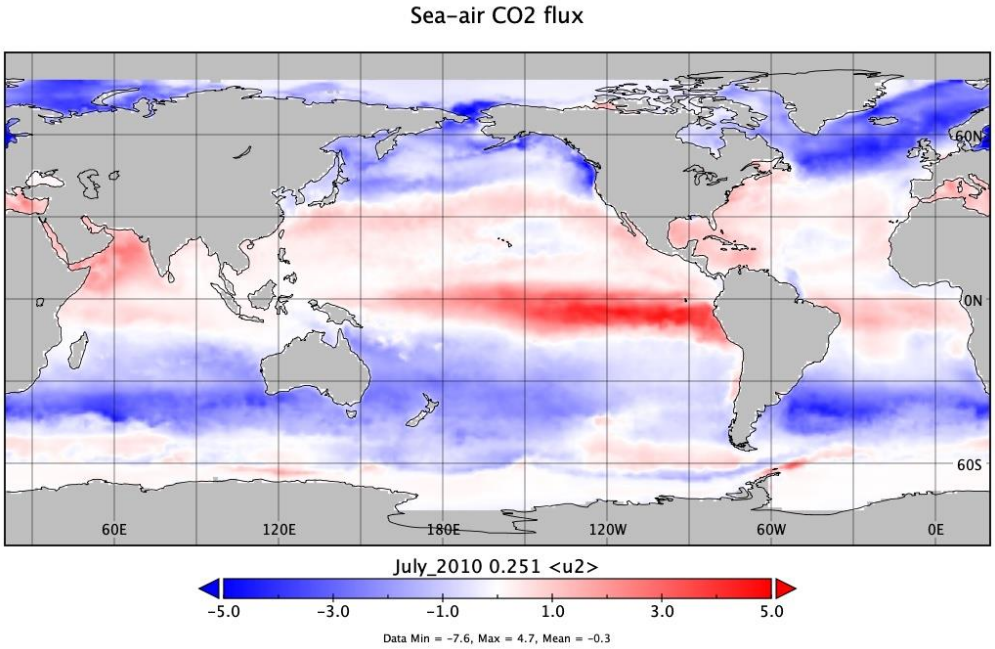

Figure 4. Flux maps for January (a) and July (b) 2010 using AOML_ET providing a visual depiction of spatial and seasonal changes for 2010. Color bar units [mol m^{-2} y^{-1}].

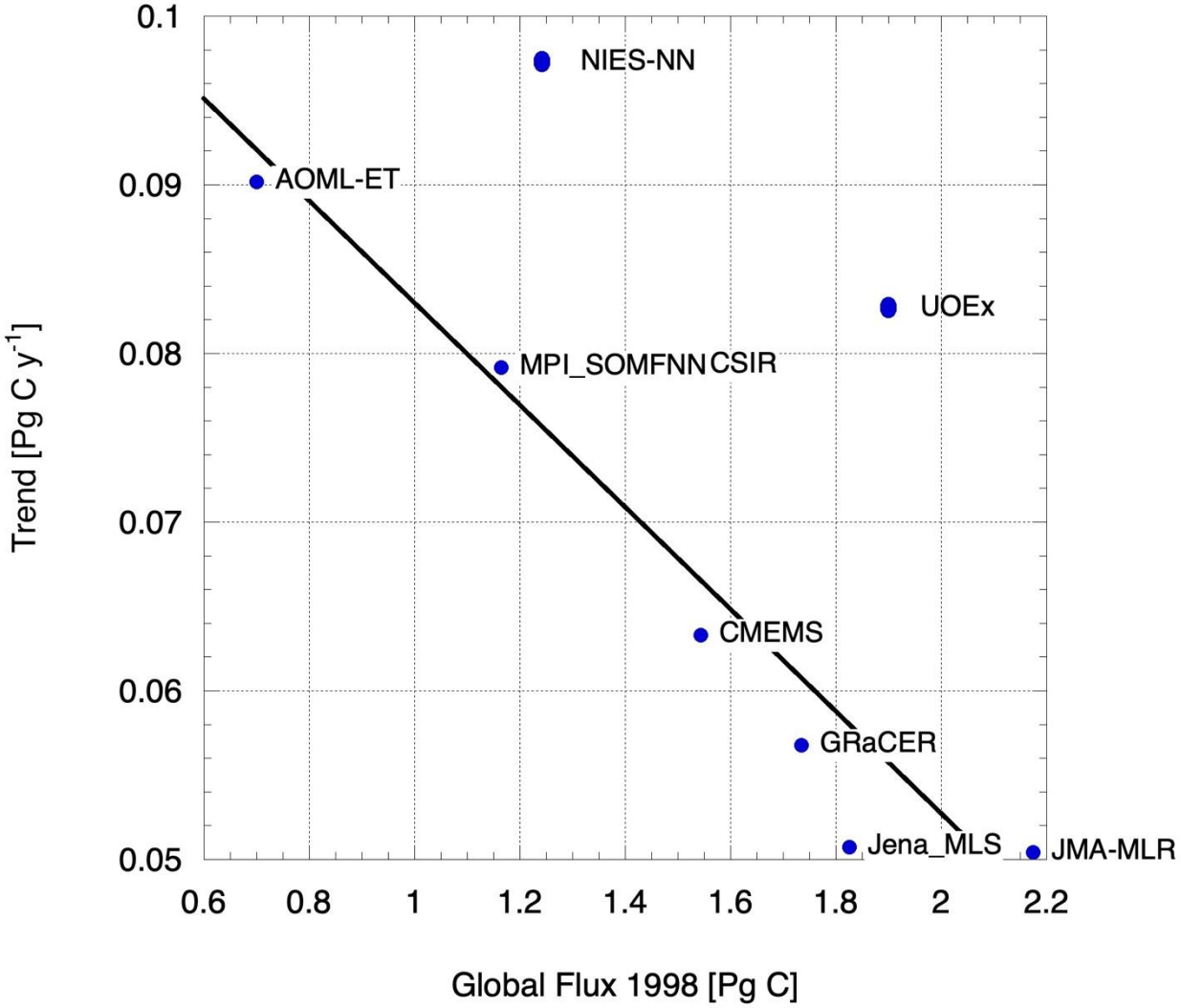

Figure 5. Relationship between global ocean CO_2 uptake in 1998 and trend from 1998 to 2020 for different ML methods. The linear relationship plotted (Trend [Pg C y^{-1}]) = 0.11 - 0.03 Flux(1998) R^2 =0.84) does not include the ML approaches of NIESS-NN and UoEx. For references of the methods see caption in Table 1.

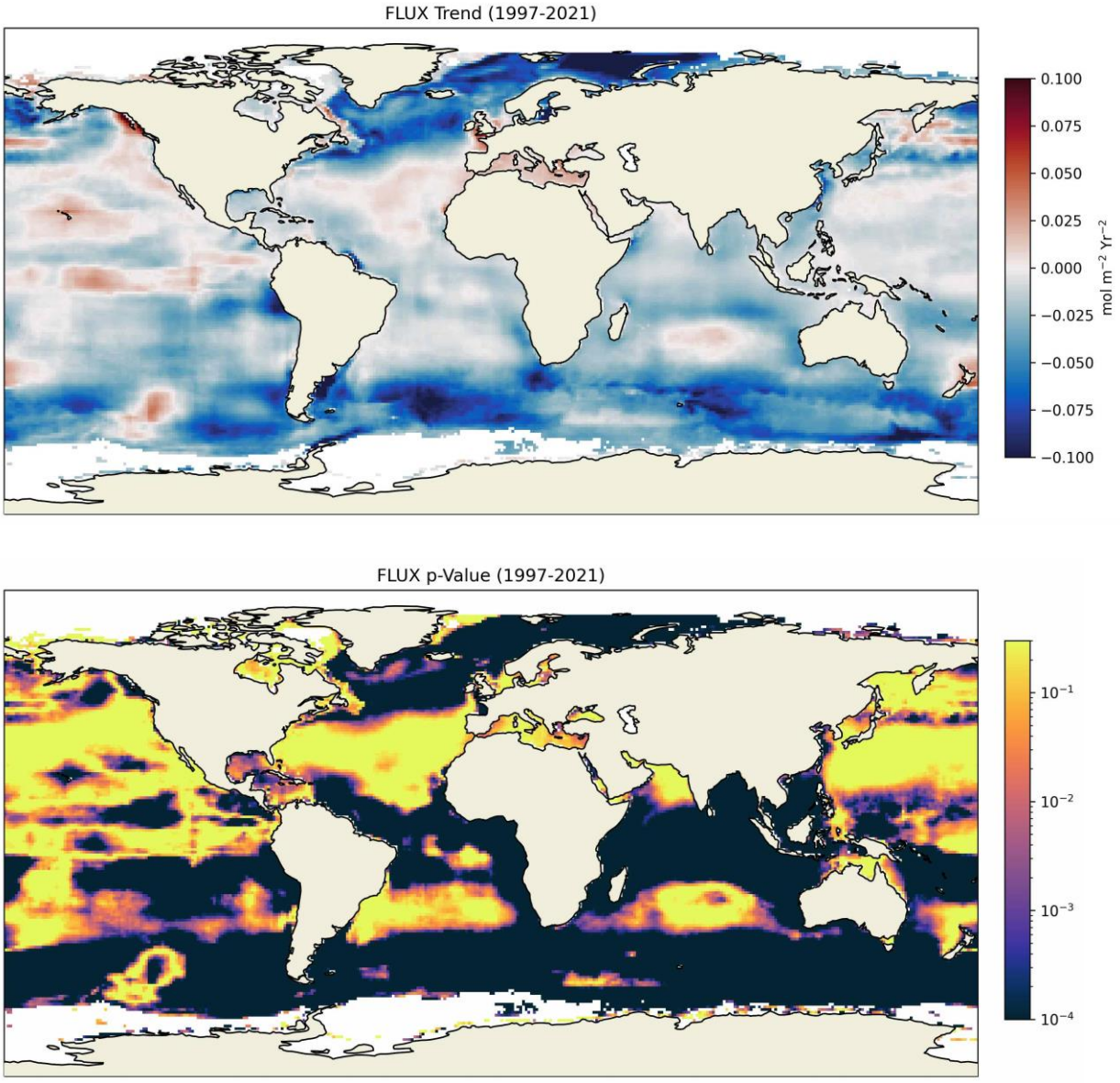

Figure 6. (a) Map of differing trends in sea-air CO_2 fluxes from 1998-2020 in mol m^{-2} y^{-2} and (b) P-values for trend for AOML_ET. The large trends both positive and negative have P values of less than 0.01 that are statistically significant.

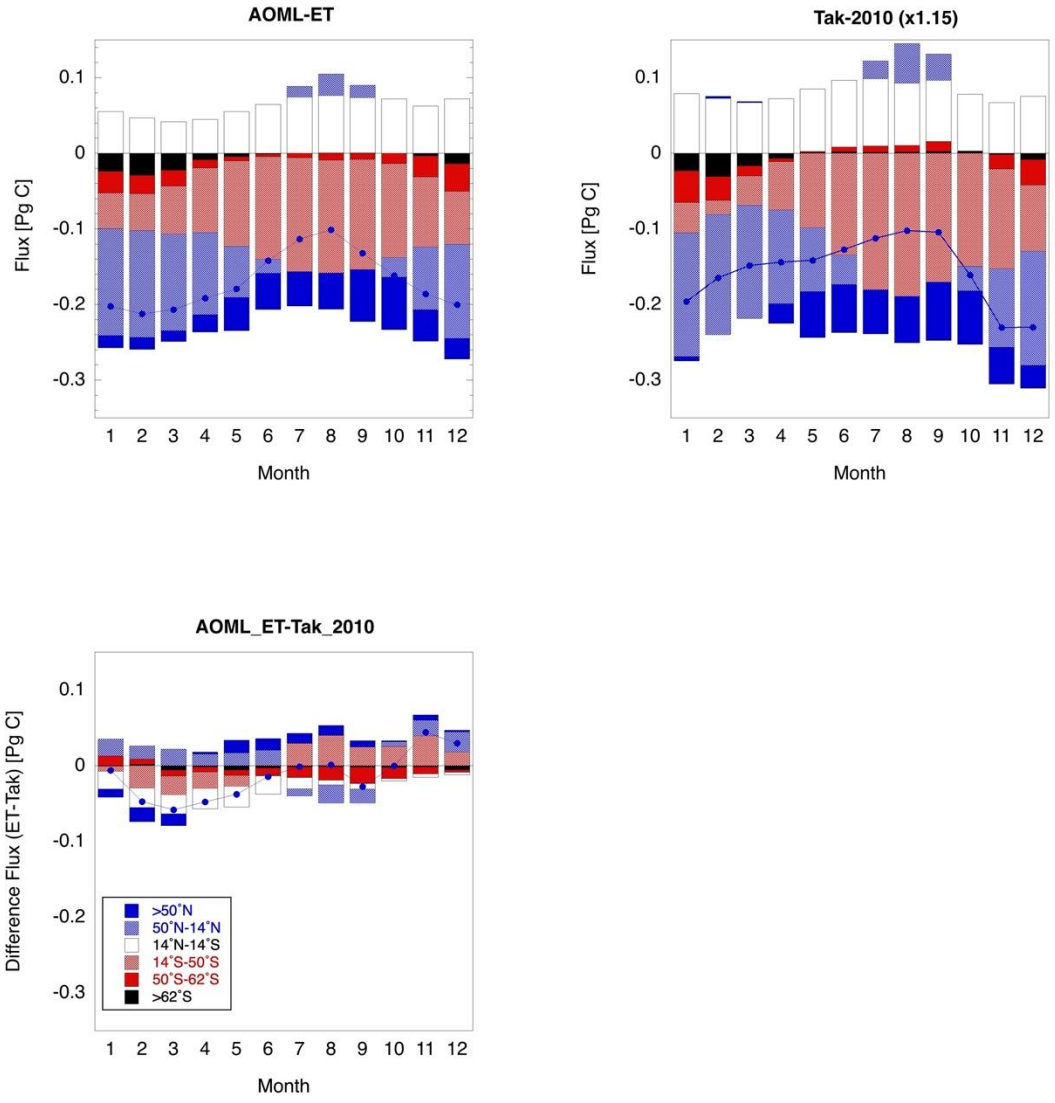

Figure 7. Regional monthly zonal fluxes based on the (a) AOML_ET effort; that of (b) Tak-2010, scaled to the same surface area (x1.15); and (c) the difference. The different zones following Takahashi et al. (2009) are listed in the legend. The lines with blue circles are the net monthly fluxes for 2010. Fluxes are expressed in [Pg C per month].

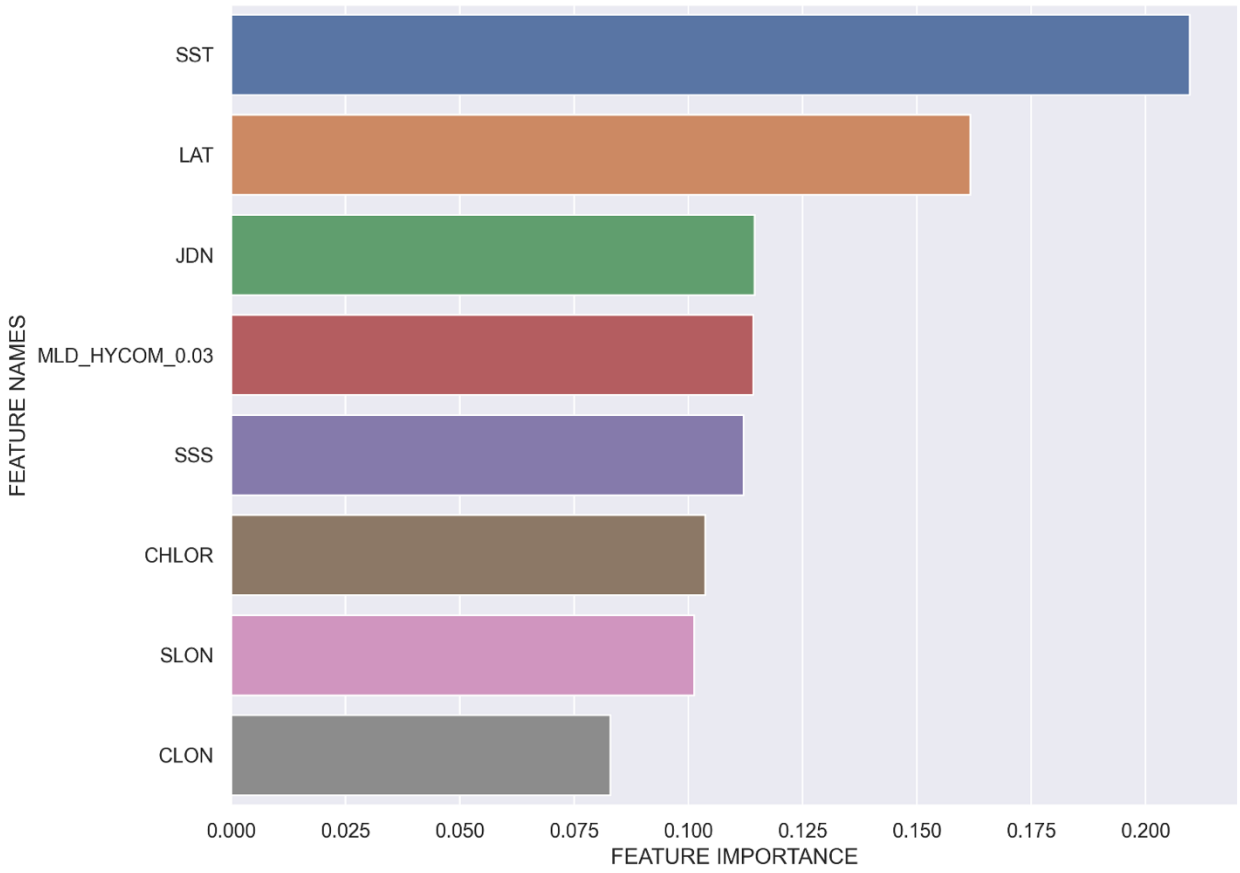

Figure 8. Importance of the different predictor variables in the AOML_ET analysis. Location (latitude (Lat), and longitude (SLON and CLON) has the greater importance for predictability followed by SST. The other products, Julian day (JDN), Mixed layer depth (MLD-Hycom _0.03), sea surface salinity (SSS) , and Chlorophyll-a (Chl-a) have similar impact.

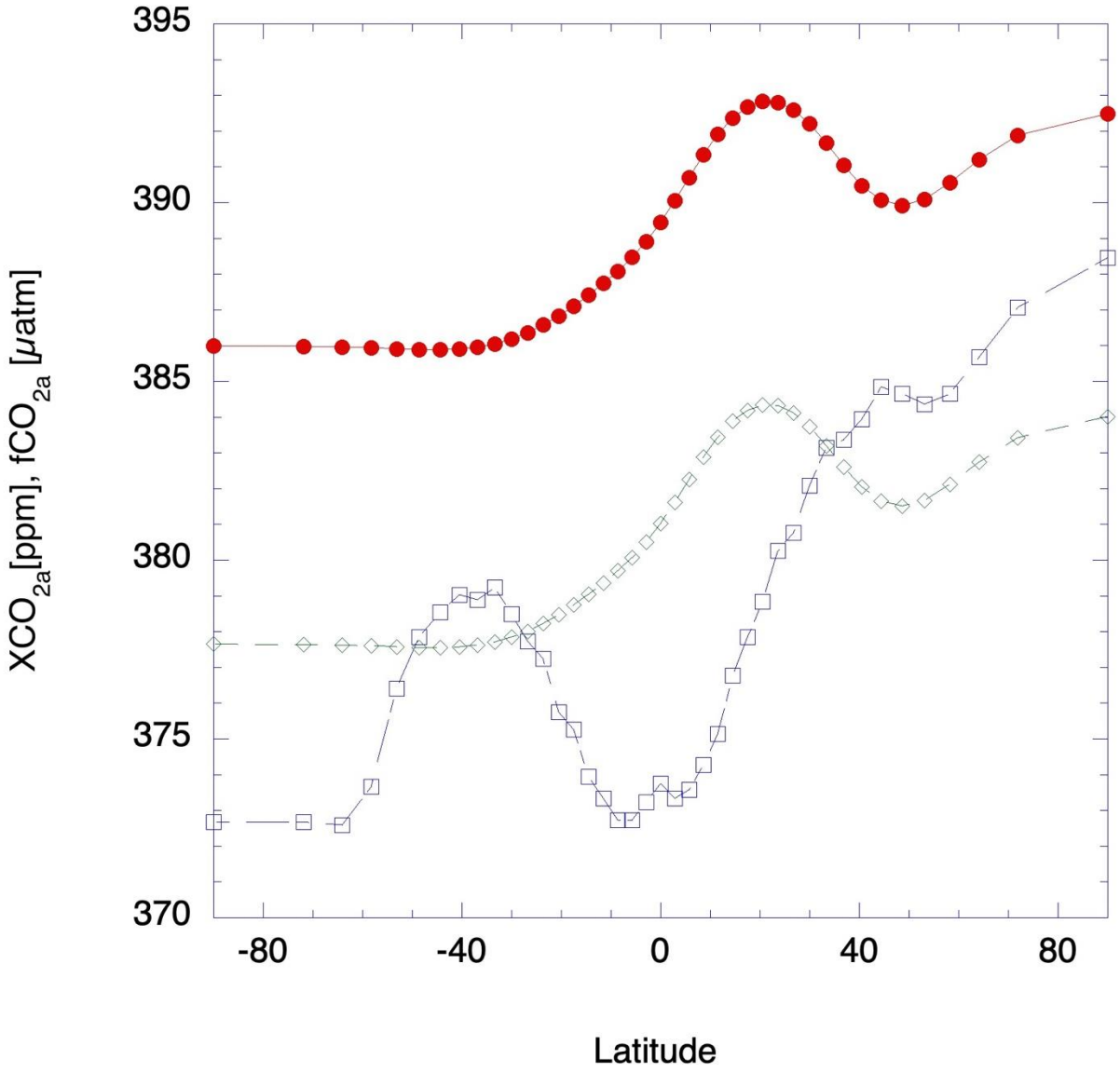

Figure 9. Zonal average XCO_{2a} (red line with circles); fCO_{2a} at fixed temperature of 16.1˚C and pressure of 1 atm (dashed green line with diamonds); and fCO_{2a} at measured temperature and pressure (dashed blue line with squares) for June 2010.

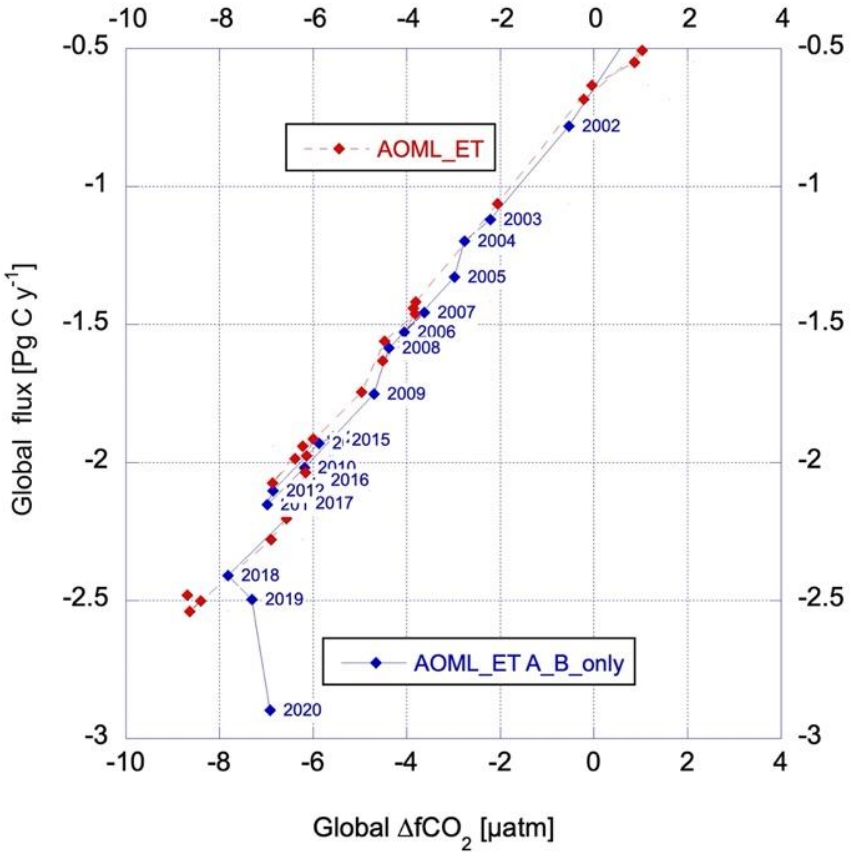

Figure 10. Global net flux for the default AOML_ET approach using data sets flagged A-D (red line), and datasets A,B (blue line) versus global average ΔfCO_2. The regression between net flux and ΔfCO_2 is 0.214 Pg C/µatm, (r^2 =0.99) for all data, and 0.227 Pg C/µatm , (r^2 =0.99) for A, B data only, omitting the datapoint for 2020.

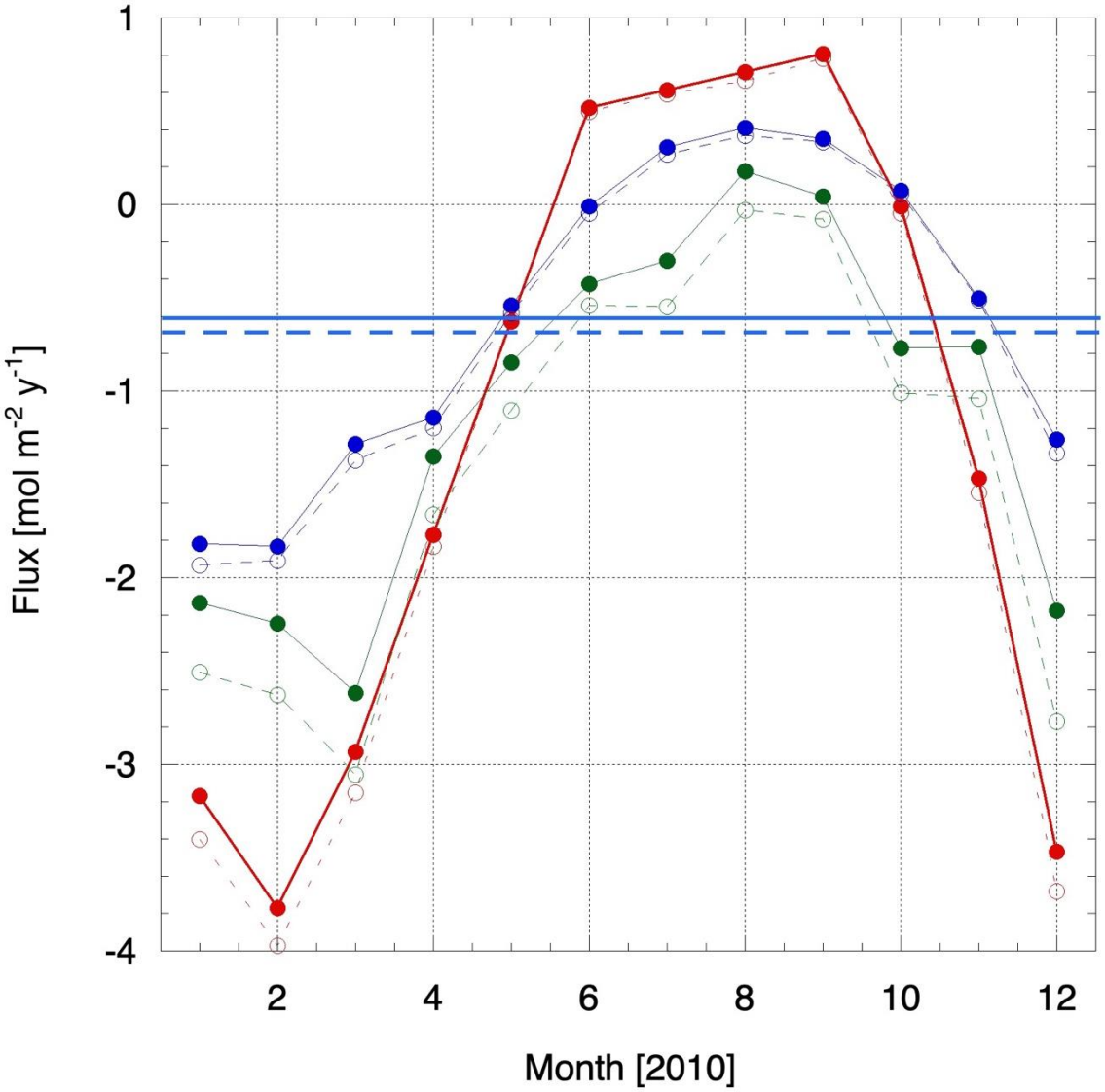

Figure 11. Monthly averaged air-sea CO_2 fluxes in the 30˚-35˚N latitude band using different XCO_{2a} products and the AOML_ET for fCO_{2w} values. The MBL XCO_{2a} product (solid line; solid circles) and PBL XCO_{2a} product (dashed lines; open circles) are shown versus month for 2010. The blue lines are zonally averaged fluxes for 30˚-35˚N ; the green lines are fluxes over the Yellow Sea (30˚-35˚N); the red lines are the fluxes over the Mid-Atlantic Bight (30˚-35˚N). The horizontal solid and dashed blue lines are the annual average fluxes using the MBL and PBL products, respectively in the 30˚-35˚N latitude band.

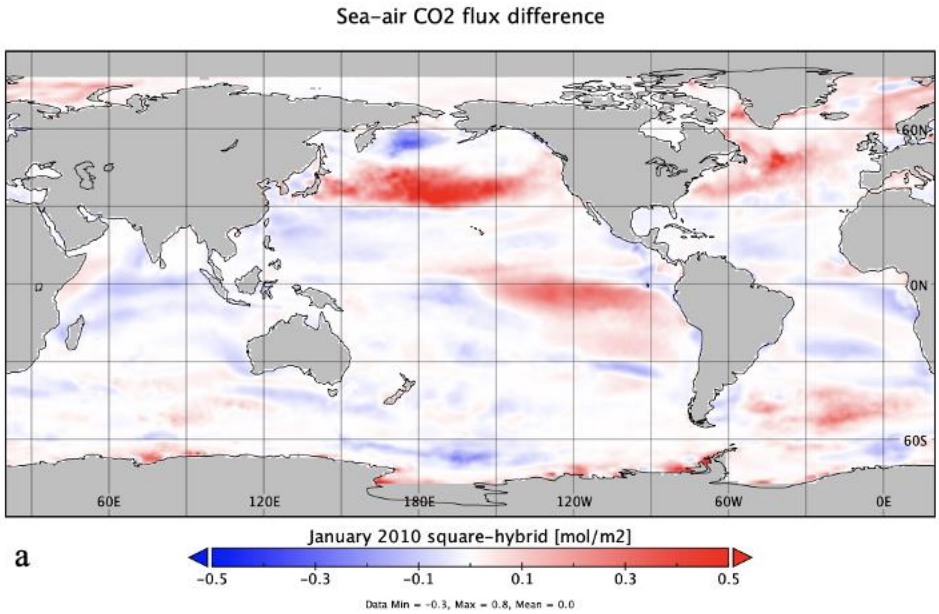

a

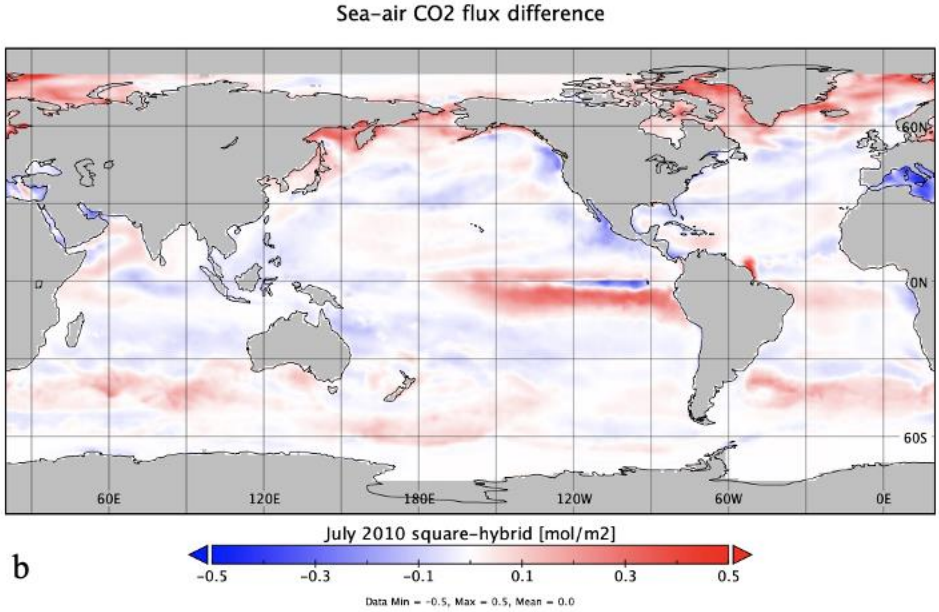

b

Figure 12. Maps of differences in air-sea CO_2 fluxes between the square wind speed and hybrid relationships for gas transfer for January (a) and July (b) 2010 using AOML_ET. The flux densities for January and July using AOML_ET and the default wind speed squared relationship are shown in Figure 4. Color bar has units of [mol m^{-2} y^{-1}].

Table 1. Summary of magnitude variability and trends of global air-sea CO_2 fluxes from different Machine Learning Approaches. Annual data from

Study[a]	Average 1998-2020[b]	Trend[c]	$r^{2,d}$	StError[e]	Flux 1998[f]	Flux 2020[g]
	Pg C	Pg C decade^{-1}		Pg C	Pg C	Pg C
AOML_ET	**-1.70**	-0.89	0.92	0.19	-0.72	-2.54
AOML_ET_ABonly	*-1.60*	*-0.97*	*0.88*	*0.25*	*-0.49*	*-2.42*
AOML_ET-Chla	*-1.82*	*-0.87*	*0.86*	*0.24*	*-0.71*	*-2.33*
AOML_ET_MLD	*-1.72*	*-0.87*	*0.88*	*0.23*	*-0.80*	*-2.28*
AOML_ET+<U^2>	*-1.72*	*-0.94*	*0.93*	*0.17*	*-0.71*	*-2.72*
AOML_ET_ΔfCO_2	*-3.60*	*-0.55*	*0.91*	*0.12*	*-3.22*	*-3.99*
MPI-SOMFFN	**-1.91**	-0.79	0.93	0.15	-1.17	-2.56
Jena-MLS	**-1.99**	-0.51	0.63	0.26	-1.83	-2.60
CMEMS	**-1.94**	-0.63	0.92	0.13	-1.54	-2.88
GRaCER	**-2.12**	-0.57	0.95	0.09	-1.74	-2.66
JMA-MLR	**-2.36**	-0.50	0.77	0.19	-2.18	-3.25
NIES_NN	**-2.01**	-0.98	0.93	0.18	-1.24	-3.42
CSIR	**-2.08**	-0.79	0.96	0.11	-1.53	-3.02
UoEx	**-2.43**	-0.83	0.92	0.17	-1.90	-2.89
Average[h]	-2.06	-0.7	0.88	0.16	-1.53	-2.87
Min.[h]	-1.70	-0.5	0.63	0.09	-0.70	-2.54
Max.[h]	-2.43	-0.98	0.96	0.26	-2.18	-3.42

a. All data, except AOML-ET are from https://globalcarbonbudget.org/carbonbudget/. AOML ET: AOML Extra Trees (this work); MPI-SOMFFN (Landschützer et al., 2016); Jena-MLS (Rödenbeck et al., 2022); CMEMS (Chau et al., 2022): GRaCER (Gregor & Gruber, 2021); NIES_NN (Zeng et al., 2014); JMA-MLR (Lida et al., 2021); CSIR(Gregor et al., 2019) UoEx (Watson et al., 2020)

b. Twenty-three year average (1998-2020) of the annual global values for each approach in Pg C

c. Trend based on a linear regression of the twenty three years of annual global air-sea CO_2 fluxes in Pg C decade^{-1}

d. Coefficient of determination

e. Standard error from the linear trend

f. Global air-sea CO_2 flux in 1998 for each of the methods

g. Global air-sea CO_2 flux in 2020 for each of the methods

h. Average, minimum, and maximum of the methods (listed in bold) excluding the permutations of AOML_ET (in italics).